Yun X, Zhu YF, Wang ZX, Gardner L. Benchmark tests on high strength steel I-section frames. Engineering Structures, (Accepted).

Benchmark tests on high strength steel I-section frames

Xiang Yun [a], Yufei Zhu [a], Zhongxing Wang [b,c], Leroy Gardner [a]

[a] *Department of Civil and Environmental Engineering, South Kensington Campus, Imperial College London, London SW7 2AZ, UK*

[b] *Key Laboratory of Earthquake Engineering Simulation and Seismic Resilience of China Earthquake Administration, Tianjin University, Tianjin 300350, PR China*

[c] *School of Civil Engineering, Tianjin University, Tianjin 300350, PR China*

Abstract

Physical experiments are widely used in structural engineering for the validation of finite element models and the establishment and assessment of design provisions. However, while there exists an abundance of member-level test data, there is a clear need for further benchmark frame-level test data, particularly given the growing trend for advanced system-level simulation and design. Towards meeting this need, and exploiting state-of-the-art measurement techniques, tests on eight high strength steel frames are presented herein. The tested frames were fixed-base, single storey, unbraced in-plane and made up of welded S690 steel I-section members. Two section sizes, of different local slenderness, were employed to assess the influence of local buckling on cross-section strength and the potential for plastic redistribution of forces within the frames. All the frames were laterally restrained out-of-plane using a bespoke lateral bracing system, but free to deform in-plane. The frames were subjected to different combinations of horizontal and vertical loading, in order for beam, sway and combined mode mechanisms to form. Extensive use was made of digital image correlation in order to obtain detailed information on the deformation of the frames and their components. The test setup, instrumentation, loading procedures and frame structural

response, including load-deformation characteristics, failure modes and connection rotational stiffnesses are fully reported. The experimental data indicated that, despite the lower ductility and strain hardening of HSS relative to normal strength steel (NSS), HSS frames with stocky cross-sections have the ability to form plastic hinges with sufficient rotation capacity to achieve a considerable amount of inelastic moment redistribution; the potential for extending plastic design to HSS structures has therefore been demonstrated. The test results also provide a firm basis for the validation of advanced numerical models and system-level design approaches.

Keywords: Benchmark tests; Digital image correlation (DIC); Experiments; High strength steel (HSS); Large-scale frame tests; Plastic design; Structural systems.

1. Introduction

High strength steels (HSS), commonly defined as steels with yield strengths over 460 MPa, are attracting increasing attention in the construction industry; their use can lead to significant weight savings, facilitating more streamlined, sustainable and economic structures. Recent years have seen a gradual but clear global trend towards the wider use of HSS in structural engineering, particularly in large structures with heavily loaded elements. Examples include the Shanghai World Financial Centre (China), Sony Centre (Germany), Yokohama Landmark Tower (Japan) and Tseung Kwan O Cross-Bay Link Bridge (China). More recent developments on the use of HSS in structural engineering can be found in Ban and Shi [1]. The use of HSS has been particularly prominent in columns in high rise buildings, with the column cross-sections tending to be relatively stocky I-sections or hollow sections to reduce susceptibility to buckling and maximise the utilization of the material strength. Alternatively, the columns can be filled with, or encased in, concrete to suppress buckling. In recent

decades, a considerable body of research has been carried out on the structural behaviour and design of HSS cross-sections and members under various loading conditions, such as by Tse et al. [2] and Yun et al. [3,4]. However, investigations into the behaviour of HSS at the structural system level remain scarce [5-9]. This has, to a certain degree, inhibited the development of design provisions for HSS in current standards, such as the European code EN 1993-1-12:2007 [10] and the American Specification AISC 360 [11], by, for example, precluding the use of plastic design.

Plastic design refers to the analysis and design approach in which a sequence of plastic hinges form in an indeterminate structural frame under increasing loading, until sufficient hinges are present to form a collapse mechanism. This design approach assumes full plastic redistribution of moments once a plastic hinge has formed, and therefore requires suitably stable moment-rotation characteristics from the constituent cross-sections of the structural members in the frame. Current European design guidance [12] ensures that these requirements are met by allowing only Class 1 cross-sections to be employed for plastic design (i.e. local buckling is controlled) and by allowing only material grades up to S460 to be used; HSS have not, to date, been considered appropriate for plastic design because of their lower ductility and lower ultimate strength to yield strength ratio f_u/f_y relative to normal strength steel, but there is a growing body of evidence to support a relaxation to the current restrictions. For example, tests on HSS beams have shown high rotation capacities, sufficient for plastic design [13,14], while tests on continuous beams have demonstrated the potential for plastic redistribution and the ability to attain full system plastic collapse loads. However, the corresponding behaviour of HSS frames is yet to be explored, and is therefore examined experimentally in the present study, allowing the interaction between plastic collapse and global instability to be assessed. Note that scarcity of test data on structural systems is not

only limited to HSS though; there is also a general dearth of high quality physical experimental results on structural steel systems. Such experimental data are much needed for the validation of advanced numerical simulations and system-level design approaches [15-21].

A comprehensive experimental study comprising tests on a total of eight steel frames made of S690 welded I-sections has been conducted in the Structures Laboratory at Imperial College London and is presented herein. Advanced experimental techniques, including digital image correlation, were employed to gain a thorough insight into the response of the tested frames. Details of the test specimens, setup and procedures are fully described, while the results are reported and analysed. The main objective of the present study is to generate experimental data on HSS indeterminate frames, which can be used in future studies as benchmarks for the validation of advanced numerical models and design approaches.

2. Experimental program

2.1. Material testing

The chemical composition of the examined S690 steel material employed in the present study, as provided by the manufacturer, is given in Table 1, and satisfies the requirements specified in EN 10025-6 [22] for quenched and tempered HSS. The key material properties and full-range stress-strain responses of the studied S690 steel were determined by tensile coupon tests. Tensile coupons were cut from the same batch of plates as employed for the fabrication of the frame specimens. Specifically, two longitudinal tensile coupons were extracted from the parent 8 mm-thick plate along its rolling direction. The dimensions of the coupon specimens complied with the requirements specified in EN ISO 6892-1 [23]. The tensile coupon tests were performed under displacement control using an Instron hydraulic 250 kN testing machine, with the displacement rate of 0.05 mm/min up to the yield strength and a

higher rate of 0.5 mm/min for the post-yield range. Two strain gauges were attached to the mid-height of the tensile coupons, one on each of the two wider faces, to measure the longitudinal tensile strain; in addition, a video extensimeter was used to measure the elongation over a gauge length of 140 mm.

The measured engineering stress-strain curves are depicted in Fig. 1, while the key average material properties, including the Young's modulus E, the yield strength f_y, the ultimate strength f_u, the strain hardening strain ε_{sh} where the yield plateau ends and subsequently the strain hardening initiates, the strain at the ultimate strength ε_u, the fracture strain ε_f (measured over the standard gauge length of $5.65\sqrt{S_0}$, where S_0 is the original cross-sectional area of the tensile coupon [23]), the ultimate-to-yield strength ratio f_u/f_y and the ultimate-to-yield strain ratio $\varepsilon_u/\varepsilon_y$ (where $\varepsilon_y = f_y/E$), are reported in Table 2. The stress-strain characteristics of the hot-rolled S690 steel used in this study are similar to those of S690 steels collected in the literature [24].

2.2. Frame specimens

A total of eight two-dimensional, single bay, single storey, unbraced rectangular frames was tested. For each of the eight tested frames, the same welded I-section was used for both the columns and beam. The frame specimens were categorized into two series, with each series consisting of four identical frames, according to their cross-section (CS) profile: Series 1 (CS1 HSS-I-65×116×8×8) and Series 2 (CS2 HSS-I-80×136×8×8). Note that the cross-sections of the frame specimens were selected so that the failure load of each frame was within the limits of the actuator capacities and the maximum deformation of each frame was less than the available stroke of the hydraulic actuators, as described in Section 3. The cross-section identifier is composed of four letters "HSS-I" designating an HSS welded I-section

made of S690 steel, followed by the nominal dimensions of the I-section in millimeters, i.e. flange width B × outer section depth H × flange thickness t_f × web thickness t_w, as illustrated in Fig. 2. The two different welded I-sections were fabricated from 8 mm-thick quenched and tempered S690 steel plates by means of gas metal arc welding with a nominal weld leg length (t_{weld}) of 5.6 mm (i.e. a weld throat thickness of 4 mm), as shown in Fig. 2. Note that the two investigated welded I-sections are both Class 1 under pure compression according to the slenderness limits specified in 1993-1-12 [10] but have different local flange and web slenderness ratios to enable the influence of local slenderness on the key issues of rotation capacity and potential for plastic redistribution to be studied.

Fig. 3 shows the configuration of the test frame specimens; the span of the frames (i.e. the distance between the column centrelines) was 3.168 m and the height of the frames (i.e. from the base of the columns to the centreline of the beam) was 2 m. The average measured geometric dimensions of the cross-section of each frame specimen are presented in Table 3; the cross-sectional properties of each frame specimen, calculated based on the average measured values, are also presented in Table 3, where A is the cross-sectional area, W_{el} and W_{pl} are the elastic and plastic section moduli, respectively, and M_{el} and M_{pl} are the elastic and plastic bending moment capacity, respectively. The frame specimens are labelled according to their cross-section profile and loading condition, as shown in Table 3, in which ‘V’ indicates that the frame is subjected to pure vertical load, ‘H’ indicates that the frame is subjected to pure horizontal load, and ‘V&H-1’ and ‘V&H-2’ indicate that the frame is subjected to combined vertical and horizontal loads, with different vertical-to-horizontal load ratios. Note that in the present study, unless otherwise stated, the cross-sectional properties are given with respect to the major axis.

All connections employed in the present test programme, including the extended end plate beam-to-column connections and the base connections (as detailed in Section 3.2), were designed to be moment-resisting and near rigid, as shown in Fig. 4. Note that in Fig. 4, the white paints on the surface of the beam-to-column connection are a speckle pattern for the digital image correlation (DIC) technique that was utilized during the frame testing to measure the full field displacement of the specimens. The beam-to-column connections comprised a 16-mm thick beam end plate, made of S690 steel, which was fillet welded to the beam end and bolted to the column flange using eighteen preloaded high strength M12 or M16 bolts for the frame specimens composed of the smaller (I-65×116×8×8) or larger (I-80×136×8×8) welded I-section, respectively. The beam end plate has a greater width than that of its connected column, thereby enabling the beam-to-column connection to be further strengthened by means of bolting the beam end plate to a strengthening plate attached to the outer side of the column flange using ten preloaded high strength M20 bolts, as illustrated in Fig. 4. Grade 8.8 bolts were used in the connections of the first tested frame specimen (i.e. HSS-I-100-65-V), while higher grade (12.9) bolts were adopted in the remaining frame test specimens. All bolts were tightened to predetermined torque values according to the requirements set out in EN 1090-2 [25]. Tightening torques of 425 Nm, 210 Nm, 88 Nm were applied to the Grade 8.8 M20, M16 and M12 bolts respectively, and 720 Nm, 350 Nm, 150 Nm to the Grade 12.9 M20, M16 and M12 bolts, respectively. Each of the M20 bolts was housed within a steel tube, positioned between the beam end plate and the stiffening plate (see Fig. 4), to prevent the inward bending of the two plates due to the preload in the M20 bolts. The dimensions and the layout of the bolts for the beam-to-column connections of the frame specimens composed of the smaller (I-65×116×8×8) and larger (I-80×136×8×8) welded I-section are shown in Figs. 5(a) and 5(b), respectively. A series of stiffeners (i.e. horizontal stiffeners, vertical stiffeners, diagonal stiffeners and beam end plate stiffeners, as

indicated in Figs. 4 and 5) were cut from 16 mm thick S690 steel plates and welded onto the frame panel zones and beam end plates to increase the strength and stiffness of the connections. Note that the presence of the beam end plate stiffeners also had the effect of shifting the plastic hinge locations away from the beam ends to the beam sections where the stiffeners terminated; the column end plate stiffeners had the same effect, as described in the next section.

An additional 10 mm-thick bearing plate was inserted between the beam end plate and the column flange for the frame specimens composed of the smaller welded I-section (I-65×116×8×8), as shown in Fig. 5(a), to maintain the same distance between the centrelines of the two columns as for the frame specimens with the larger welded I-section (I-80×136×8×8); this also aided the installation process.

3. Frame test setup and instrumentation

The schematic solidworks model of the frame test setup is shown in Fig. 6. The test rig contained three main hydraulic actuators, four external support frames and top and bottom loading beams, as illustrated in Fig. 6.

3.1. Loading conditions

Different loading conditions were applied to the four frame specimens within each of the two test series, with one subjected to vertical load V only applied at the mid-span of the beam, one subjected to horizontal load H only applied to the bottom loading beam and the other two subjected to different combinations of the two (V and H). For the frames subjected to combined loading, the vertical load V_{test} was first applied at the mid-span of the beam until the pre-determined load was reached (i.e. 100 kN and 130 kN for HSS-I-65×116-V&H-1 and

HSS-I-65×116-V&H-2 respectively and 150 kN and 210 kN for HSS-I-80×136-V&H-1 and HSS-I-80×136-V&H-2 respectively). The vertical load V_{test} was then held constant while the horizontal load H_{test} was applied at the column base through the bottom loading beam until either collapse of the frame or excessive deformation occurred. For all the frame tests, the vertical load was applied under load control at a slow rate of approximately 5 kN/min, while the horizontal load was introduced under displacement control at approximately 2 mm/min.

The vertical load was applied using two 232 kN (25 tonne) hydraulic actuators, which were mounted on the bottom flange of the top loading beam, in alignment with the mid-span of the beam of the frame specimen. The top loading beam was a 250 × 250 × 8 mm cold-formed S700 steel square hollow section (SHS), which was fixed to the vertical support frame, as shown in Fig. 6. The two vertical hydraulic actuators, placed next to each other in parallel, were fed by a single pump in order to ensure even loading. The vertical load was measured using a calibrated load cell positioned under the vertical hydraulic actuators and applied through a steel roller, as shown in Fig. 7. A pair of stiffeners was welded to the frame specimen at the vertical loading point to prevent web crippling due to the concentrated vertical load, as also shown in Fig. 7.

The horizontal load was applied to the bottom loading beam by a 250 kN hydraulic actuator, as shown in Fig. 8, which was mounted on the left horizontal support frame, as illustrated in Fig. 6. The frame specimens were fixed to the bottom loading beam, which was seated on several greased roller bearings, allowing the frames to move in-plane with minimal friction. The frame specimens were horizontally restrained at the top of the right-hand column (see Figs. 6 and 9) by a horizontal support. The horizontal support included a manual hydraulic pump, a bearing plate and a set of steel rollers, as illustrated in Fig. 9. The manual hydraulic pump was fixed to

the bearing plate, and the pump head (featuring the roller bearings) was attached to the surface of the strengthening plate prior to testing, as shown in Fig. 9(a). For the frame specimens that were loaded horizontally, the manual hydraulic pump was used to adjust the position of the bearing plate such that it remained vertical during testing, as shown in Fig. 9(b); this ensured that the reaction remained horizontal, despite the rotation of the right-hand beam-to-column connection. The load provided by the manual hydraulic pump was increased as the horizontal load increased, approximately to half of the applied horizontal load. The horizontal support provided a "hinge-like" boundary condition at the top of the right-hand column. The horizontal load was applied at the base level, allowing the vertical actuator to remain stationary during testing, rather than requiring it to move laterally with the frame. This loading configuration is statically equivalent to applying the horizontal load at the right-hand beam-to-column connection and restraining lateral movements at the column bases. Note that the bottom loading beam was of the same cross-section profile as the top loading beam, but was filled with concrete to prevent any local failure of the tube due to the concentrated loading.

3.2. Load cells

Three specially fabricated load cells, similar to those used by Young and Rasmussen [26] and Arrayago et al. [27], were employed to measure the reaction forces and moments at the column bases. Each of the load cells consisted of two 38 mm-thick steel plates and four cylindrical steel studs (80 mm in depth and 50 mm in diameter) welded in between the two plates, as illustrated in Fig. 10. Each of the four steel studs was equipped with four strain gauges, as shown in Fig. 10, to measure the longitudinal strains at different locations; these strains were used to determine the applied load and bending moment.

The load cells were calibrated prior to fixing them to the frames. Two load cells were used to measure the vertical reaction loads and bending moments at the column bases as shown in Fig.

11(a), while a third load cell was welded into the middle of the bottom loading beam, as shown in Fig. 11(b), to determine the horizontal reaction loads (i.e. shear forces) at the column bases. As illustrated in Fig. 12, the end plate of each column was bolted to the fabricated load cell using four Grade 8.8 M16 bolts. The bottom load cell plate at each column base was welded to the bottom loading beam, as shown in Fig. 11(a). To enhance the rigidity of the column base connections, a 38 mm-thick U-shaped strengthening plate made of S355 steel was placed on top of each column end plate and bolted to the top load cell plate by means of four Grade 8.8 M30 bolts, and stiffeners were also welded at each column base to strengthen the column end plates, as shown in Fig. 12.

3.3. Lateral restraints

A bespoke restraint system was designed to prevent out-of-plane instability of the test frames without inducing any undesirable in-plane restraint. The restraint system comprised a total of 14 out-of-plane lateral restraints, among which 6 were used to provide lateral restraint to the beam of the test frames and 4 provided lateral restraint to each column, as shown in Fig. 6. Each out-of-plane lateral restraint comprised two tee-shaped plates which were placed on either side of the web of the beam or column section of the frame specimens and connected using two M30 bolts, and a bracing member comprising two parallel S460 SHS 50×50×6.3 arms, as shown in Fig. 13. The assembled tee-shaped plates were connected to the bracing member using an M24 bolt, which was greased to facilitate free rotation. Two 35 mm diameter Macalloy bars, as shown in Fig. 13, were also employed in each lateral restraint; one allowed adjustment of the length of the lateral restraint as well as the rotation of the lateral restraint about the axis of the bar, while the other permitted the horizontal (for column lateral restraints) or vertical (for beam lateral restraints) movement of the lateral restraint as the frame specimen deformed during testing. A ratchet spanner was used to rotate the threaded

bar manually, thereby enabling the horizontal (or vertical) movement of the lateral restraints to match that of the frames during testing, as shown in Fig. 14.

A spirit level was placed on each beam lateral restraint to facilitate adjustment to ensure the restraint remained horizontal throughout testing. Similarly, the column lateral restraints were moved along with the displacements of the columns of the frame specimens at the corresponding heights. Fig. 15 illustrates the methodology for ensuring the alignment of the column lateral restraint and the corresponding position on the column of the frame specimen. A pair of matching color-coded 'rainbow' rulers with lines at 2 mm intervals were mounted to both ends of each column lateral restraint, and a laser level was employed to generate the vertical line on the rulers. The restraints were adjusted such that the matching colors were aligned, ensuring that that restraints remained perpendicular to the plane of the frames. The adopted restraint system and the continuous manual adjustment approach throughout testing ensured that lateral restraint was provided to the frames, while minimizing any influence on the in-plane response.

Out-of-plane lateral restraint was also provided at the top end of each column through a pair of bearing plates fastened to the top loading beam, as shown in Fig. 16. A specially devised roller bearing was fixed to the top of each column, the displacement of which was constrained to remain in-plane by the bearing plates. Specifically, the roller bearing was welded to a fabricated clamp, placed on the top of each column, which was composed of three steel plates and had an I-shaped groove at the bottom to accommodate the top end section of the column. The roller bearing was used in order to allow the frame specimen to deform in-plane with minimum, if any, friction being generated.

3.4. Instrumentation

Electrical resistance strain gauges were mounted on the top and bottom flanges at selected locations on the frame specimens to estimate bending moments and monitor the strain development histories during testing. As indicated in Fig. 3, a total of eight beam and column sections (Section 1-1 to Section 8-8 in Fig. 3) were monitored, located adjacent to (i.e. at a distance of 50 mm from the corresponding stiffened section) the base of each frame column, the beam-to-column connections and the mid-span of the beam, covering the most highly stressed regions of the frames under the different loading scenarios. String potentiometers (SP) were used to measure the in-plane vertical deflections at the mid-span of the beam (see SP3 in Fig. 3) and the in-plane horizontal deflections at the base and top of each column (see SP1, SP2, SP4 and SP5 in Fig. 3). Note that SP4 was placed below the strengthening plate of the right-hand beam-to-column connection for the frame specimens subjected to horizontal loading to avoid conflict with the horizontal restraint system. In addition, a total of six inclinometers (I) was employed on each frame, positioned close to the beam-to-column connections and the column base connections, as illustrated in Fig. 3, to measure the rotation of the connections and to evaluate their rotational stiffnesses. The test outputs, including the applied loads and displacements from the hydraulic actuators, as well as the readings from the strain gauges, string potentiometers and inclinometers, were continuously monitored and recorded at 1-s intervals using the data acquisition system DATASCAN.

3.5. Digital Image Correlation (DIC)

Digital Image Correlation (DIC) was also employed to provide more comprehensive displacement and strain measurements. Compared with conventional instrumentation (e.g. strain gauges, transducers and inclinometers) which is commonly used to monitor deformations at key discrete locations, DIC enables full-field measurements to be captured,

making it ideal for use in structural testing. A four-camera LaVision DIC system was used for the image acquisition, as shown in Fig. 17, among which two cameras with 8 mm focal length lenses (Cameras 1 and 2 in Fig. 17) were used to monitor the deformation fields of the full frame specimens, while the other two cameras (Cameras 3 and 4 in Fig. 17), which were equipped with longer focal length lenses of 35 mm to ensure sufficient resolution, were employed to record the surface strain field at the most highly stressed region (i.e. the region where the first plastic hinge formed), which could be either at the base of one column or at the mid-span of the beam depending on the loading scenario, throughout testing. Prior to testing, the front surface of all frame specimens was sprayed with a thin layer of black paint, on top of which different random white speckle patterns were drawn in order to achieve an average speckle size of 3-5 pixels in the acquired images from the two pairs of cameras. Consequently, a fine speckle pattern was applied to the most highly stressed region of each frame while a relatively coarse speckle pattern was used elsewhere, as illustrated in Fig. 17. The output signals from the horizontal and vertical hydraulic actuators were fed into the DIC system through an analogue-to-digital converter, while images were captured at 2-s intervals and processed using the DaVis version 8.4.0 imaging software (LaVision 2017 [28]). The measurements from the strain gauges, string potentiometers and inclinometers, as described in the previous subsection, were used to corroborate the DIC measurements at key locations, as discussed in the next section.

3.6. Imperfection measurements

The initial imperfections of the assembled frame specimens, including out-of-plumbness of the frames, as well as out-of-straightness of the members, were measured. Plumb and horizontal lines were generated using a laser adjacent to the columns and beams of the frame specimens, respectively, to serve as reference lines from which deviations could be measured

at a series of different locations, marked with cross-shaped points in Fig. 18. The resulting initial in-plane imperfection measurements for all the frames are shown in Fig. 18.

According to EN 1090-2:2018 [25], the mean inclination of all the columns in the same single storey of a building should be less than a prescribed erection tolerance of $h/500$, where h is the height of the column in metres. For the studied frames, this corresponds to the sum of the sway imperfection amplitudes of the left-hand and right-hand columns being less than 8 mm; this was achieved for all frames except for frame specimen HSS-I-65×116-V&H-1. The initial out-of-plane imperfections were also measured using the same method as described above, while the lateral positions of the frame specimens were adjusted using the lateral restraints (through the Macalloy bars positioned within the length of the lateral restraints, as shown in Fig. 13) to ensure that the amplitudes of the out-of-plane imperfections were less than 2 mm for all frame specimens. These small amplitudes of out-of-plane imperfections, coupled with the fact that the frame specimens were laterally restrained throughout the testing, meant that the out-of-plane imperfections and deformations were considered to have negligible influence on the structural performance of the tested frame specimens.

4. Test observations and discussion

The key results measured from the frame experiments, including the ultimate collapse loads, failure modes, load-deformation histories and rotational stiffnesses of the different connections, are presented and discussed in this section.

4.1. Ultimate collapse loads

Table 4 summarizes the maximum vertical loads (or the pre-determined vertical loads for the frame specimens subjected to combined loading) $V_{test,max}$ and the corresponding vertical

displacements at the mid-span of the beam of the frame specimens δ_{mid}, as well as the maximum horizontal loads $H_{test,max}$ and the corresponding horizontal displacements at the column bases δ_{base}. Note that the frame specimens subjected to horizontal load only (i.e. HSS-I-65×116-H and HSS-I-80×136-H) were terminated before reaching their ultimate loads due to the limited stroke of the horizontal hydraulic actuator of 250 mm; however, these maximum recorded loads ($H_{test,max}$) were deemed to be close to their corresponding ultimate loads since the tangent stiffnesses of the load-displacement curves at the corresponding maximum recorded load were approaching zero [29], as shown in Subsection 4.3.2.

4.2. Failure modes

4.2.1. Frame specimens subjected to vertical load only

The failure modes of the tested frame specimens subjected to vertical load only featured a beam collapse mechanism in which significant plastic deformations were observed at the mid-span of the beam (i.e. the position where the vertical load was applied) and adjacent to the beam-to-column connections, as displayed in Fig. 19. The maximum measured tensile strain occurred at the bottom flange adjacent to the mid-span of the beam (as obtained from the strain gauge readings of either SG8 or SG10, as illustrated in Fig. 3), and reached about 8.5% and 6.9% for specimens HSS-I-65×116-V and HSS-I-80×136-V, respectively, as listed in Table 5, all far in excess of the yield strain of 0.37% measured from the tensile coupon tests. Large tensile strains were also measured at the outer flanges of the columns adjacent to the beam-to-column connections (i.e. SG3 at Section 2-2 and SG13 at Section 7-7, as illustrated in Fig. 3), with maximum tensile strains attained up to 3.1% and 2.0% (again, well in excess of the yield strain) for specimens HSS-I-65×116-V and HSS-I-80×136-V, respectively, as listed in Table 5. Note that the maximum measured tensile strains from the pair of sections located adjacent to the beam-to-column connections (i.e. Section 2-2 and

Section 3-3, and Section 6-6 and Section 7-7 as illustrated in Fig. 3) as well as the mid-span of the beam (i.e. Section 4-4 and Section 5-5 as illustrated in Fig. 3) are listed in Table 5, where the lower values are shown in brackets.

4.2.2. Frame specimens subjected to horizontal load only

The test specimens subjected to horizontal load only failed due to material yielding, the spread of plasticity and the formation of a sway plastic collapse mechanism, as shown in Fig. 20 and discussed below. The maximum tensile strains were recorded from the strain gauges located adjacent to the base of the columns (i.e. SG2 at Section 1-1 and SG15 at Section 8-8, as illustrated in Fig. 3), with the maximum tensile strain measured from SG15 being slightly larger than that from SG2, reaching approximately 5.4% and 7.0% for frame specimens HSS-I-65×116-H and HSS-I-80×136-H, respectively, as given in Table 5. The measured maximum tensile strains at the locations adjacent to the beam-to-column connections (i.e. Sections 2-2, 3-3, 6-6 and 7-7, as illustrated in Fig. 3) were all beyond the measured yield strain of 0.37%, indicating yielding had occurred at these positions prior to failure. The maximum tensile strains in the beam sections adjacent to the beam-to-column connections (i.e. SG5 at Section 3-3 and SG12 at Section 6-6, as illustrated in Fig. 3) were generally greater than those recorded in the column sections adjacent to the corresponding beam-to-column connections (i.e. SG3 at Section 2-2 and SG14 at Section 7-7, as illustrated in Fig. 3); the maximum measured tensile strains from SG5 were approximately 1.0% and 2.2% for frame specimens HSS-I-65×116-H and HSS-I-80×136-H, respectively, while the maximum measured tensile strains from SG12 reached about 1.4% and 1.9% for frame specimens HSS-I-65×116-H and HSS-I-80×136-H, respectively, as tabulated in Table 5. The attainment of high strains adjacent to the column bases and to the beam-to-column connections signifies the development of plastic hinges and the formation of the sway plastic collapse mechanism.

4.2.3. Frame specimens subjected to combined loading

For each test series, two frame specimens were tested under different combinations of horizontal and vertical loads. The failure modes of these frame specimens were characterized by a combined beam and sway plastic collapse mechanism, as shown in Figs. 21 and 22, but with different hinge formation sequences owing to the different loading conditions, as given in Table 4. The tensile strain at the bottom flange adjacent to the mid-span of the beam for frame specimen HSS-I-65×116-V&H-1 (taken as the average strain from the pair of SG8 and SG10, illustrated in Fig. 3) reached 0.29% when the predetermined vertical load $V_{test,max}$, as given in Table 4, was applied, which was lower than the measured yield strain of 0.37% indicating that the stresses within the section at the mid-span of the beam remained relatively low prior to the introduction of the horizontal load. However, for the other three frame specimens, first yield occurred at the mid-span of the beam prior to the horizontal load being applied, with the maximum average tensile strains (from the pair of SG8 and SG10) being 0.7%, 0.9% and 1.7% for frame specimens HSS-I-65×116-V&H-2, HSS-I-80×136-V&H-1 and HSS-I-80×136-V&H-2, respectively, when the corresponding predetermined vertical load $V_{test,max}$ was reached. For all four frame specimens subjected to combined loading, different degrees of plastic deformation, as reflected by the maximum tensile strains reported in Table 5 and shown in the failure modes of Figs. 21 and 22, occurred at the mid-span of the beam, the column bases and adjacent to the left-hand beam-to-column connection, while the sections adjacent to the right-hand beam-to-column connection remained elastic, since they experienced relatively small levels of bending moment and compression in the combined load cases. The observed order of yielding was generally consistent with the anticipated sequence of plastic hinges determined from a first order plastic analysis.

4.3. Load versus displacement curves

The load versus displacement curves are presented in Figs. 23-25 for the frame specimens subjected to vertical load only, horizontal load only and combined loading, respectively. The sequence of the formation of the plastic hinges (PH) and the locations of the formed plastic hinges are also indicated in Figs. 23-25. Herein, a plastic hinge is deemed to have formed when the maximum tensile strain within the cross-section reaches three times the yield strain (i.e. $3\varepsilon_y = 1.11\%$).

4.3.1. Frame specimens subjected to vertical load only

The relationships between the vertical applied load and the vertical displacement at the mid-span of the beam for the frame specimens subjected to vertical load only are plotted in Fig. 23. The initial stiffness of frame HSS-I-65×116-V was lower than that of frame HSS-I-80×136-V due to the smaller cross-section size, and the ultimate resistance was about 40% lower compared to that of HSS-I-80×136-V, as shown in Table 4.

4.3.2. Frame specimens subjected to horizontal load only

Fig. 24 shows the responses of the frame specimens subjected to horizontal load only in terms of the horizontal applied load versus the horizontal displacement at the column bases. Note that, for all frame specimens subjected to horizontal load, the difference between the horizontal applied load and the corresponding horizontal reaction load measured by the load cell placed within the horizontal support system was typically less than 5%. As shown in Fig. 24, frame specimen HSS-I-65×116-H, with smaller cross-section dimensions, had a lower initial stiffness and ultimate resistance compared to those of specimen HSS-I-80×136-H.

4.3.3. Frame specimens subjected to combined loading

Both the vertical and horizontal responses of the frame specimens subjected to combined

vertical and horizontal loads are plotted in Fig. 25. The load-displacement curves for the frame specimens within each series subjected to vertical load or horizontal load only are also plotted in Fig. 25 for comparison purposes. As shown in Fig. 25, during the vertical loading step, which was always first, the vertical applied load versus the vertical displacement curves for the frame specimens subjected to combined loading conditions follow those of the corresponding frame specimens under vertical load only. The vertical load in the first combined loading case of each test series (i.e. HSS-I-65×116-V&H-1 and HSS-I-80×136-V&H-1) was relatively small, thus the vertical response of the frame specimens under the first combined loading cases was almost linear during the vertical loading step; however, the vertical load in the second combined loading case of each test series (i.e. HSS-I-65×116-V&H-2 and HSS-I-80×136-V&H-2) was large enough to result in yielding at the mid-span of the beam prior to the introduction of the horizontal load. During the horizontal loading step, the vertical load remained constant while the vertical displacement at the mid-span of the beam grew as the horizontal load increased, as shown in Fig. 25. The presence of the vertical load for the frame specimens subjected to combined loading conditions led to a degradation of both strength and stiffness compared to those of the corresponding frame specimens subjected to horizontal load only, with the larger vertical load (i.e. the second combined loading case of each test series) resulting in greater loss of resistance and stiffness, as shown in Fig. 25. Owing to the relatively high level of vertical load $V_{test,max}$ for frame specimen HSS-I-80×136-V&H-2, the first plastic hinge at the mid-span of the beam (Section 5-5) formed when the horizontal load had reached only about 40% of the maximum applied horizontal load $H_{test,max}$, as indicated in Fig. 25(b). The maximum strain at the first plastic hinge continued to increase under increasing load, allowing moment redistribution and the formation of subsequent plastic hinges. The peak load of the system was reached prior to the full development of the final plastic hinge as judged based on the strain gauge data relative to $3\varepsilon_y$, though there was, nonetheless, clear plastification in this region; this may have been due to some unloading at the location of the first plastic hinge or in the top-left region of the frame that experienced some out-of-plane deformation.

4.4. DIC results and connection rotational stiffness

In this subsection, the DIC measurements are firstly compared with the relevant measurements from the conventional instrumentation, confirming the accuracy of the DIC technique. The DIC measured displacement fields, longitudinal strain fields and displacements at specific points of interest, which cannot be easily measured using conventional techniques, are then presented and analysed to provide a better understanding of the structural behaviour of the investigated HSS frame specimens.

4.4.1. DIC validation and results

To confirm the accuracy of the results obtained from the DIC system, the DIC measurements were compared with the relevant measurements from the strain gauges, inclinometers and string potentiometers. As detailed earlier, two cameras with 8 mm focal length lenses (Camera 1 and 2 indicated in Fig. 17) were used to monitor the deformation fields of the full frame specimens; the displacement and rotation responses determined based on the images captured by the two cameras were compared to those measured from the string potentiometers and inclinometers, respectively, at the corresponding location of each frame specimen. Load-deformation histories obtained from the DIC system and the conventional instrumentation show excellent agreement, examples of which are shown in Fig. 26 for frame specimens HSS-I-80×136-V and HSS-I-80×136-H. The histories of strain development at the most highly stressed region of each frame specimen measured from the DIC (using images taken from Camera 3 and 4 shown in Fig. 17) and strain gauges are also compared; good agreement was also observed, as seen from the typical comparison shown in Fig. 27. Overall, it may be concluded that the DIC system employed in the present study provides accurate and reliable measurements of both the overall deformation of the full frame specimens and the strain development histories at the most highly stressed region of each frame specimen.

The maximum out-of-plane displacement that occurred in any frame was smaller than 20 mm, confirming the generally effectiveness of the lateral restrain system. The location of the maximum out-of-plane displacement was typically in the heavily stressed top left region of the frames, where the lateral restraint spacing was slightly higher than elsewhere, although the lateral torsional buckling slenderness $\bar{\lambda}_{LT}$ of the unrestrained member length remained below 0.2. The out-of-plane displacement fields obtained from the DIC for two typical frame specimens (specimens HSS-I-80×136-H and HSS-I-65×116-V&H-1) at the maximum applied load, together with the load versus out-of-plane displacement curves at the critical region (i.e. the region where the maximum out-of-plane displacement occurred), are displayed in Fig. 28. Note that the positive and negative out-of-plane displacements in Fig. 28 represent movements toward and away from the DIC system, respectively, with reference to Fig. 17. The maximum out-of-plane displacement arose in the top left region of the frames as a consequence of inelastic local buckling, accompanied with some minor influence from inelastic lateral torsional buckling, while no significant out-of-plane displacement was observed in the remaining regions. It should be noted that it is not practically possible to have zero out-of-plane deformation for structural testing at large-scale. To reduce out-of-plane deformation further, even closer lateral restraint spacing could be used, but care must be taken not to restrain local buckling and not to provide excessive lateral restraint that does not reflect practical arrangements.

The longitudinal strain fields in the DIC monitored region (using images taken from Camera 3 and 4 shown in Fig. 17) at two representative load levels: (a) the load at which the maximum strain within the DIC monitored region reached approximately the yield strain, and (b) the maximum applied load, are displayed for three typical frame specimens in Fig. 29.

The spread of plasticity with the increase in applied load in the DIC monitored region can be clearly seen by the quantitative change in the strain fields, as shown in Fig. 29.

4.4.2. Connection rotation stiffness

The moment-rotation characteristics of the connections in the frame specimens, including the beam-to-column connections and the column base connections, were carefully analysed using the data measured by strain gauges, inclinometers and the DIC system at relevant locations to determine their moment-rotation response.

Extended end-plate joints, as shown in Fig. 5, were used for the beam-to-column connections. The rotation of the strengthening plate θ_{col+pz} included that of both the column θ_{col} and the panel zone θ_{pz} caused by shear deformation, as schematically illustrated in Fig. 30. The horizontal displacements at two marked regions on the strengthening plate (i.e. identified by the blue points shown in Fig. 30) were measured by the DIC system. The rotation of the strengthening plate θ_{col+pz} was determined using Eq. (1), where d_1 and d_2 are the DIC measured horizontal displacements at the top and bottom marked regions of the strengthening plate, respectively, and d_3 is the distance between the two marked points, as illustrated in Fig. 30. The rotation at the beam end θ_b was measured using the inclinometer positioned at the web of the beam section close to the beam-to-column connection (i.e. using inclinometer I1 for the left-hand beam-to-column connection and inclinometer I3 for the right-hand beam-to-column connection), as shown in Fig. 30. The connection rotation θ_c was finally calculated by subtracting the rotation of the strengthening plate θ_{col+pz} and the rotation resulting from beam flexure $\theta_{b,flex}$ (but this was very small and is not discussed further) from the rotation at the beam end θ_b, as given in Eq. (2).

$$\theta_{col+pz} = \arctan\left|\frac{d_1 - d_2}{d_3}\right| \quad (1)$$

$$\theta_c = \theta_b - \theta_{col+pz} - \theta_{b,flex} \tag{2}$$

In the elastic region, the bending moments at the eight monitored beam or column sections, as shown in Fig. 3, can be determined by Eq. (3), based on the assumptions that all the welded I-sections remained plane and the strains were linearly distributed throughout the depth of each cross-section.

$$M_i = \frac{EI\left|\varepsilon_{max,i} - \varepsilon_{min,i}\right|}{H} \tag{3}$$

In Eq. (3), M_i is the bending moment at the i-th monitored cross-section, I and H are the second moment of area about the major axis and the depth of the cross-section, respectively, and $\varepsilon_{i,max}$ and $\varepsilon_{i,min}$ are the measured maximum and minimum strains at the extreme fibers of the i-th monitored section, respectively. The bending moment at the left-hand beam-to-column connection M_c can be determined by linear interpolation between the two calculated bending moments at Sections 3-3 and 4-4, as shown in Fig. 31; similarly, the calculated bending moments at Sections 5-5 and 6-6 (see Fig. 3) were used to determine the bending moment at the right-hand beam-to-column connection for each frame specimen. Fig. 32 shows a typical moment (M_c)-rotation (θ_c) curve for the left-hand beam-to-column connection of frame specimen HSS-I-80×136-H; the moment (M_c)-rotation (θ_c) curve of the strengthening plate as well as the moment (M_c)-rotation (θ_b) curve at the beam end θ_b are also plotted in Fig. 32. The rotational stiffness of the beam-to-column connection is taken as the slope of the regression line fitted to the elastic region of the moment (M_c)-rotation (θ_c) curve, as illustrated in Fig. 32. The undulations in the obtain moment-rotation curves for the beam-to-column connection, as shown in Fig. 32, and the column-base connection, as described

later and shown in Fig. 33, resulted from noise in the strain gauge readings. The estimated beam-to-column connection rotational stiffness for each frame specimen (taken as the average value of the left- and right-hand beam-to-column connections) is reported in Table 6.

The rotation of each column-base connection θ_{cb} was measured using the inclinometer positioned on the web of the column section close to the column-base connection (i.e. using inclinometer I5 for the left-hand column-base connection and I6 for the right-hand column-base connection, as shown in Fig. 3). The bending moment at each column base M_{cb} was obtained from the load cell positioned beneath the corresponding column. Fig. 33 shows a typical moment (M_{cb})-rotation (θ_{cb}) curve for the left-hand column-base connection of frame specimen HSS-I-80×136-H. The estimated column-base connection rotational stiffness for each frame specimen (taken as the average value of the left- and right-hand column-base connections) is also reported in Table 6. It can be observed from Table 6 that the measured rotational stiffnesses for the connections with the same configurations (i.e. for each frame series) are quite similar, except for the beam-to-column connections of the first tested frame specimen HSS-I-65×116-V, which have a lower average rotational stiffness than their counterparts in the remaining frame test specimens of Series 1. This is attributed to the adoption of lower grade bolts (Grade 8.8 bolts instead of Grade 12.9 bolts for the remaining frame test specimens) and a lower applied pretension in the assembly of the beam-to-column connections in the first frame specimen HSS-I-100-65-V. Based on the joint classification rules set out in EN 1993-1-8:2005 [30], all connections employed in the test frame specimens are semi-rigid, except for the beam-to-column connections of frames HSS-I-65×116-H, HSS-I-65×116-V&H-1 and HSS-I-65×116-V&H-2, which are rigid.

5. Analysis and discussions

The presented test results indicate that a considerable amount of inelastic moment

redistribution can be achieved within HSS frames comprising compact cross-sections. However, plastic design of indeterminate HSS structures is not permitted in current design specifications [10,11] owing to an absence of supporting structural performance data, and the capacity of the studied HSS frames with stocky welded I-sections is limited to the load level at which the plastic moment resistance is first reached (i.e. the first plastic hinge forms), as determined by elastic analysis.

The ratios of the experimental ultimate load F_u, taken as the maximum applied vertical ($V_{test,max}$) or horizontal ($H_{test,max}$) load, as listed in Table 4, to the first order first plastic hinge load F_{1st_hinge} are plotted against the elastic critical load factor α_{cr} for all the tested frame specimens in Fig. 34. The elastic critical load factor α_{cr} indicates the susceptibility of a steel frame to the global second order sway effects and is defined as the ratio of the elastic critical load F_{cr} that causes frame buckling in an in-plane global (sway) mode to the applied design load F_d. The second order effects due to the global geometrical nonlinearity are deemed to be sufficiently small to be ignored when $\alpha_{cr} \geq 10$ according to EN 1993-1-12:2007 [10], the limit of which is also plotted in Fig. 34. For each frame, the value of α_{cr} was determined using linear buckling analysis of the frame under the loading corresponding to the ultimate stage of the test [16,31,33]; the α_{cr} of all tested frame specimens are greater than 10, indicating that the second order effects may be neglected. Thus, first order plastic analysis was performed to examine the effect of the inelastic moment redistribution in the tested HSS frame structures. The values of F_{1st_hinge} was calculated by means of first order plastic analysis (i.e. materially nonlinear analysis MNA) [31], assuming proportional horizontal-vertical loading in the ratio of $H_{test,max}/V_{test,max}$ for the frame specimens subjected to combined loading. The semi-rigid connections of the tested frame specimens were considered in the analyses by incorporating spring elements, with their rotational stiffness taken as the corresponding values measured from

the frame experiments as summarized in Table 6, into the FE models; the modelling approach has been successfully employed by [31]. It can be observed from Fig. 34 that the F_u/F_{1st_hinge} ratios ranged from 1.15 to 1.39, indicating that the current first plastic hinge (i.e. elastic) design approach [10,11] provides overly conservative resistance predictions for HSS frames with compact cross-sections due to the preclusion of the inelastic moment redistribution. The ratios of F_u/F_{1st_hinge} for the HSS-I-65×116×8×8 frames are generally higher than those of the HSS-I-80×136×8×8 frames; this is attributed to the more compact nature of the former cross-section (with the nominal flange width-to-thickness ratio being 2.86 for HSS-I-65×116×8×8 and 3.80 for HSS-I-80×136×8×8 and the nominal web width-to-thickness ratio being 11.10 for HSS-I-65×116×8×8 and 13.60 for HSS-I-80×136×8×8) having higher rotation capacity and hence a higher degree of inelastic moment redistribution. Hence, as expected, for frame specimens with the same geometries and boundary conditions and subjected to the same loading configuration, those made up with stockier cross-sections would possess higher ductility than those with slenderer cross-sections. The comparisons demonstrate the available ductility and highlight the potential for plastic design of HSS structures with compact cross-sections. It should be noted that the frame over-strength F_u/F_{1st_hinge} depends on several parameters, such as the frame geometry, boundary conditions, loading conditions and material properties; further investigation on this topic is deemed necessary through a numerical parametric study.

The ratios of the experimental ultimate load F_u to the first order plastic load F_{1st_pl} obtained from a first order plastic analysis are plotted against the elastic critical load factor α_{cr} for all the tested frame specimens in Fig. 35. For frames designed using plastic analysis, a higher limit of $\alpha_{cr} \geq 15$, beyond which second order effects may be neglected, is defined in EN 1993-1-1:2005 [12], taking account of the fact that plastically-designed steel frames are more susceptible to second order effects due to their reduced stiffness caused by the spread of plasticity and the

formation of plastic hinges [32,33]. It may be concluded from Fig. 35 that the current plastic design methods set out in EN 1993-1-1:2005 [12] are generally suitable for HSS frames, though the limit of α_{cr} = 15 above which second order effects can be ignored for plastic analysis is somewhat crude and results in slightly unconservative results for frame specimens HSS-I-80×136-V&H-1 and HSS-I-80×136-V&H-2. The ductility and plastic design of HSS frames will be investigated further in the future work by means of a numerical parametric study.

6. Conclusions

A comprehensive experimental investigation into the structural behaviour of HSS frames made of S690 welded I-sections has been presented in this paper. A total of eight two-dimensional, single bay, single storey, unbraced rectangular HSS frames were tested. The experimental setup, including the implementation of different loading schemes, the use of a bespoke restraint system to prevent out-of-plane instability and the application of specially fabricated load cells to measure the reaction forces and bending moments at the supports of the frame specimens, has been described. The supporting system was carefully designed to ensure the proper functionality of the experimental setup, which is considered to be essential in carrying out large-scale structural testing. It is hoped that the test setup presented in this article will help steer future research in structural testing, particularly in the case of steel frame testing at large-scales. Moreover, the advantages of using the DIC technique in large-scale structural testing have been demonstrated in the present study; the DIC was shown to be able to provide accurate, reliable and detailed information concerning the fields of displacement and strain both within regions of particular interest and for the overall tested system. The ultimate collapse loads, load-deformation characteristics and failure modes of the frames, together with the rotational stiffnesses of the connections, have been carefully presented and analysed. The experimental results indicated that, despite the lower ductility

and strain hardening of HSS relative to normal strength steel (NSS), HSS frames with stocky cross-sections have the ability to form plastic hinges and achieve a considerable amount of inelastic moment redistribution. In addition, it was found that the current elastic design approach as employed in EN 1993-1-12:2007 [10] provides overly conservative resistance predictions for HSS frames made of Class 1 S690 welded I-sections, while the plastic design approach set out in EN 1993-1-1:2005 [12] for normal strength steel that allows for moment redistribution at the global system level results in more accurate resistance predictions. The available ductility and potential for plastic design of HSS structures has been highlighted and will be examined further in the future work. The presented experimental investigation of HSS frames at the structural system level have allowed the assessment of the interaction between plastic collapse and global instability, and provide benchmark results that are suitable for the validation of finite element models and the development of system-level design approaches.

Acknowledgement

This projects has received funding from the Research Fund for Coal and Steel under grant agreement No 743504. The authors would also like to thank Mr. Les Clark and Ms. Sophie Day for their assistance during the experiments.

References

[1] Ban H, Shi G. A review of research on high-strength steel structures. P I Civil Eng-Str B 2018;171(8):625-641.

[2] Tse K, Wang J, Yun X. Structural behaviour and continuous strength method design of high strength steel non-slender welded I-section beam–columns. Thin-Walled Struct 2021;169:108273.

[3] Yun X, Meng X, Gardner L. Design of cold-formed steel SHS and RHS beam-columns considering the influence of steel grade. Thin-Walled Struct 2022;171:108600.

[4] Yun X, Wang Z, Gardner L. Structural performance and design of hot-rolled steel SHS and RHS under combined axial compression and bending. Structures 2020;27:1289-1298.

[5] Chen Y, Ke K. Seismic performance of high-strength-steel frame equipped with sacrificial beams of non-compact sections in energy dissipation bays. Thin-Walled Struct 2019; 139: 169-185.

[6] Wang F, Su M, Hong M, Guo Y, Li S. Cyclic behaviour of Y-shaped eccentrically braced frames fabricated with high-strength steel composite. J Constr Steel Res 2016;120:176-187.

[7] Gkantou M, Theofanous M, Baniotopoulos C. Plastic design of hot-finished high strength steel continuous beams. Thin-Walled Struct 2018;133:85-95.

[8] Hu F, Shi G, Shi Y. Experimental study on seismic behavior of high strength steel frames: global response. Eng Struct 2017; 131:163-179.

[9] Yun X, Gardner L. Numerical modelling and design of hot-rolled and cold-formed steel continuous beams with tubular cross-sections. Thin-Walled Struct 2018;132:574-584.

[10] EN 1993-1-12:2007, Eurocode 3: Design of Steel Structures − Part 1-12: Additional rules for the extension of EN 1993 up to Grades S700. European Committee for Standardization (CEN), Brussels, Belgium, 2007.

[11] ANSI/AISC 360-16, Specification for Structural Steel Buildings. American Institute of Steel Construction (AISC), Chicago, IL, 2016.

[12] EN 1993-1-1:2005, Eurocode 3: Design of Steel Structure – Part 1–1: General rules and rules for buildings. European Committee for Standardization (CEN), Brussels, Belgium, 2005.

[13] Wang J, Afshan S, Gkantou M, Theofanous M, Baniotopoulos C, Gardner L. Flexural behaviour of hot-finished high strength steel square and rectangular hollow sections. J Constr Steel Res 2016;121:97-109.

[14] Bartsch H, Eyben F, Pauli G, Schaffrath S, Feldmann M. Experimental and numerical investigations on the rotation capacity of high-strength steel beams. J Struct Eng 2021;147(6):04021067.

[15] Chan SL, Huang HY, Fang LX. Advanced analysis of imperfect portal frames with semirigid base connections. J Eng Mech 2005;131(6):633-640.

[16] Fieber A, Gardner L, Macorini L. Structural steel design using second-order inelastic analysis with strain limits. J Constr Steel Res 2020;168:105980.

[17] Gardner L, Yun X, Fieber A, Macorini L. Steel design by advanced analysis: material modeling and strain limits. Engineering 2019;5(2):243-249.

[18] Kucukler M, Gardner L, Macorini L. Development and assessment of a practical stiffness reduction method for the in-plane design of steel frames. J Constr Steel Res 2016;126: 187-200.

[19] Rasmussen KJR, Zhang H. Design of cold-formed steel single C-section portal frames. J Constr Steel Res 2019;162:105722.

[20] Ziemian RD, McGuire W, Deierlein GG. Inelastic limit states design. Part I: Planar frame studies. J Struct Eng 1992;118(9):2532-2549.

[21] Ziemian RD, McGuire W, Deierlein GG. Inelastic limit states design. Part II: Three-dimensional frame study. J Struct Eng 1992;118(9):2550-2568.

[22] EN 10025-6:2004, Hot rolled products of structural steels – Part 1: Technical delivery conditions for flat products of high yield strength structural steels in the quenched and tempered condition. European Committee for Standardization (CEN), Brussels, Belgium, 2004.

[23] EN ISO 6892-1:2016, Metallic Materials: Tensile Testing – Part 1: Method of test at room temperature. European Committee for Standardization (CEN), Brussels, Belgium, 2016.

[24] Yun X, Gardner L. Stress-strain curves for hot-rolled steels. J Constr Steel Res 2017;133:36-46.

[25] EN 1090-2:2018, Execution of steel structures and aluminium structures – Part 2: Technical requirements for steel structures. European Committee for Standardization (CEN), Brussels, Belgium, 2018.

[26] Young B, Rasmussen KJR. Measurement techniques in the testing of thin-walled structural members. Exp Mech 2003;43(1):32-38.

[27] Arrayago I, González-de-León I, Real E, Mirambell E. Tests on stainless steel frames. Part I: Preliminary tests and experimental set-up. Thin-Walled Struct 2020;157:107005.

[28] LaVision. DaVis imaging software. Ypsilanti, MI: LaVision, 2007.

[29] dos Santos GB, Gardner L, Kucukler M. A method for the numerical derivation of plastic collapse loads. Thin-Walled Struct 2018;124:258-277.

[30] EN 1993-1-8:2005, Eurocode 3: Design of steel structures − Part 1-8: Design of joints. European Committee for Standardization (CEN), Brussels, Belgium, 2005.

[31] Arrayago I, González-de-León I, Real E, Mirambell E. Tests on stainless steel frames. Part II: Results and analysis. Thin-Walled Struct 2020;157:107006.

[32] Walport F, Gardner L, Nethercot D A. A method for the treatment of second order effects in plastically-designed steel frames. Eng Struct 2019;200:109516.

[33] Walport F, Gardner L, Real E, Arrayago I, Nethercot DA. Effects of material nonlinearity on the global analysis and stability of stainless steel frames. J Constr Steel Res 2019;152: 173-182.

Figures

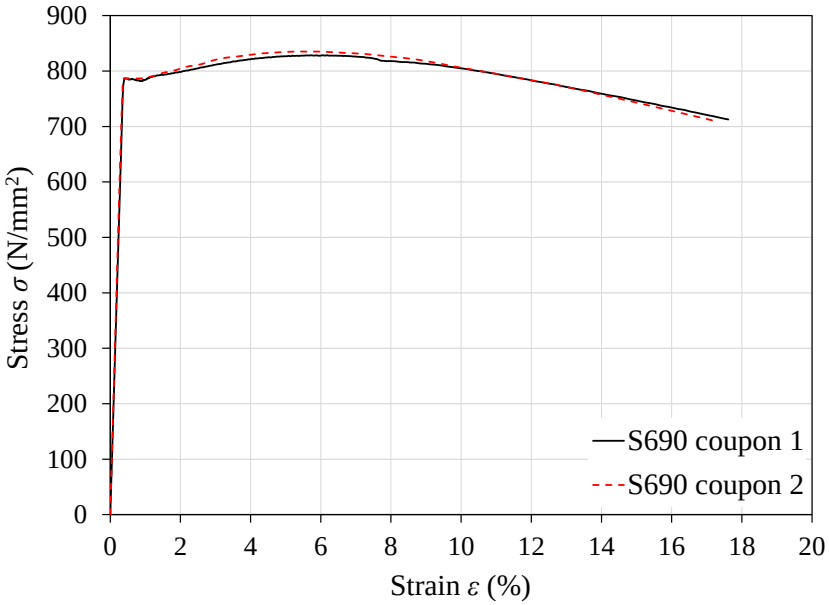


Fig. 1. Engineering stress-strain curves obtained from tensile coupon tests.

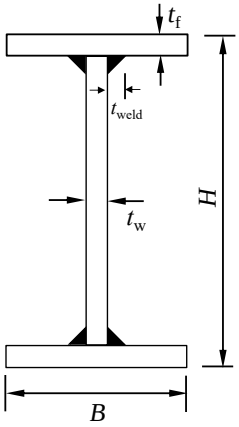


Fig. 2. Notation of welded I-sections.

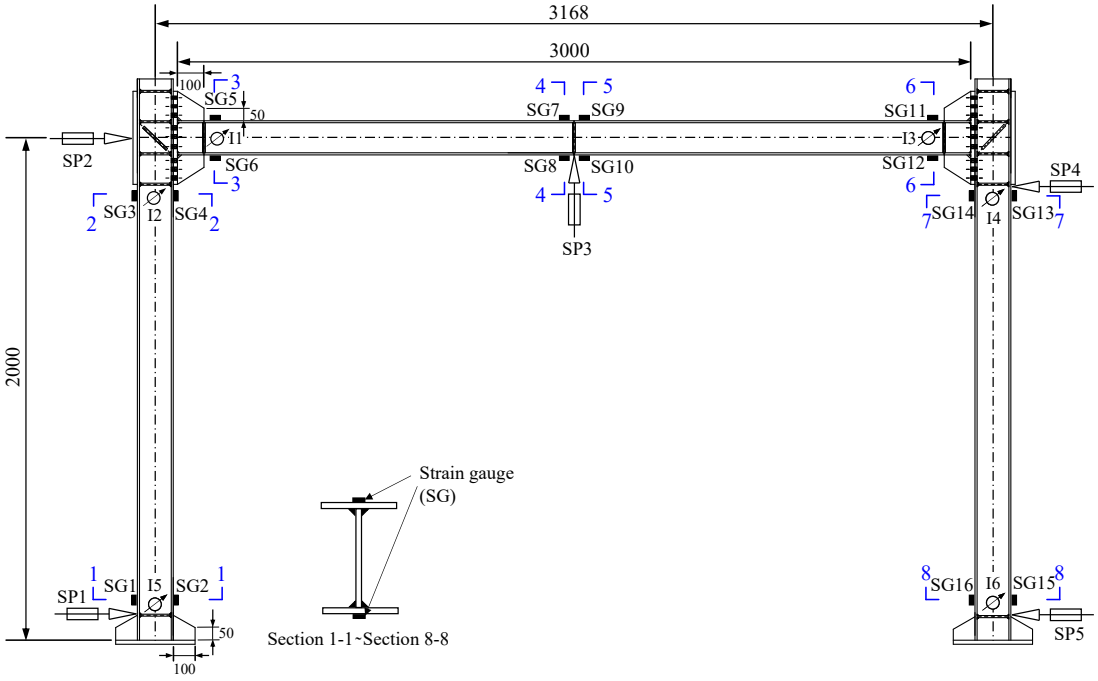


Fig. 3. Configuration of frame specimens and instrumentation, including strain gauges (SG), string potentiometers (SP) and inclinometers (I). Dimensions are shown in mm.

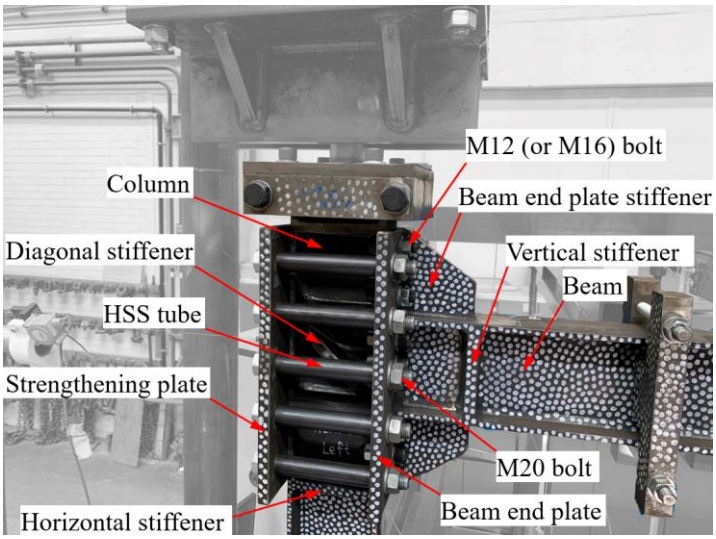
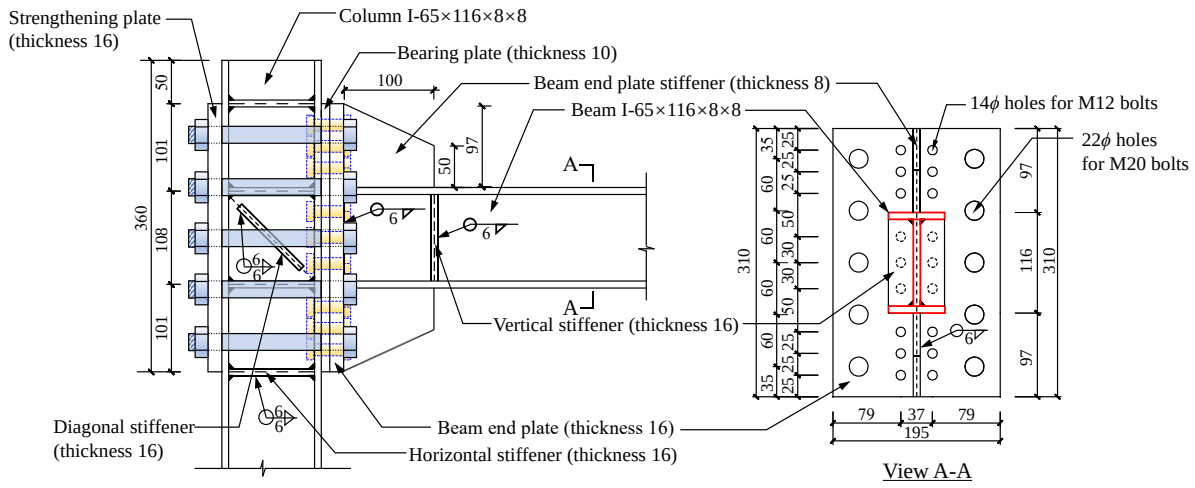
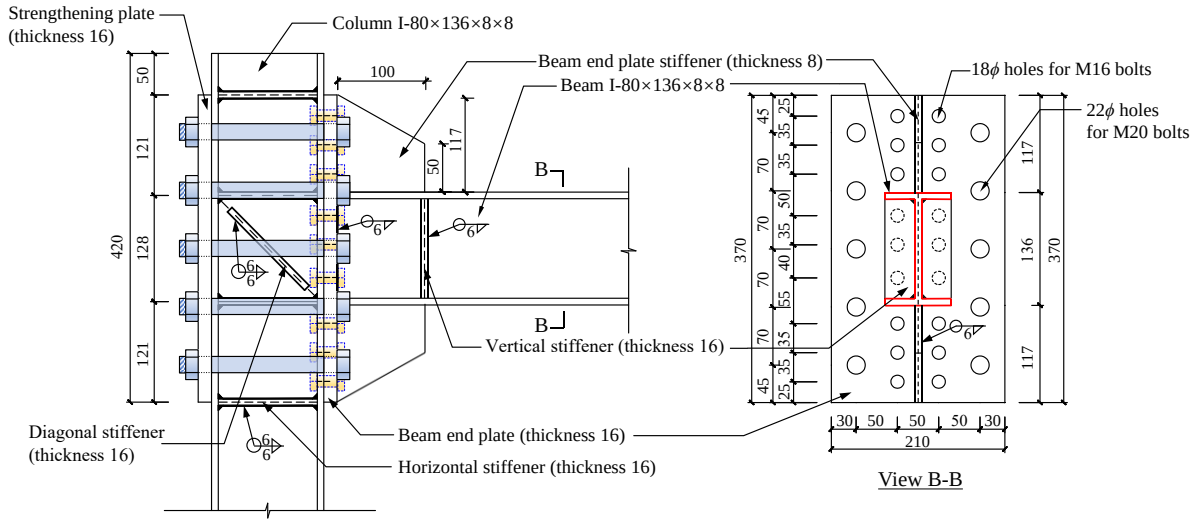


Fig. 4. Beam-to-column connection.



(a)



(b)

Fig. 5. Configurations of beam-to-column connections for frame specimens composed of (a) I-65×116×8×8; and (b) I-80×136×8×8 cross-sections (unit: mm).

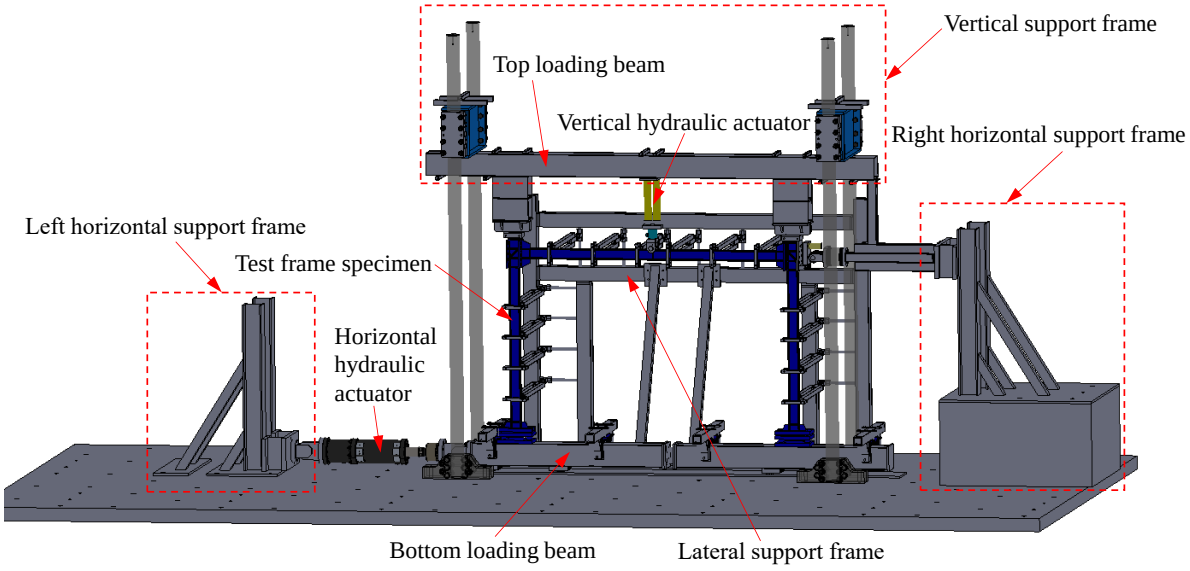


Fig. 6. Schematic solidworks model of frame test setup.

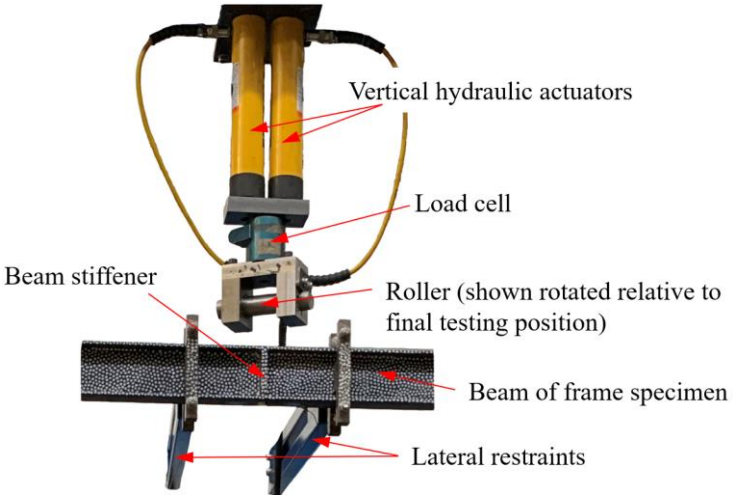


Fig. 7. Vertical loading system.

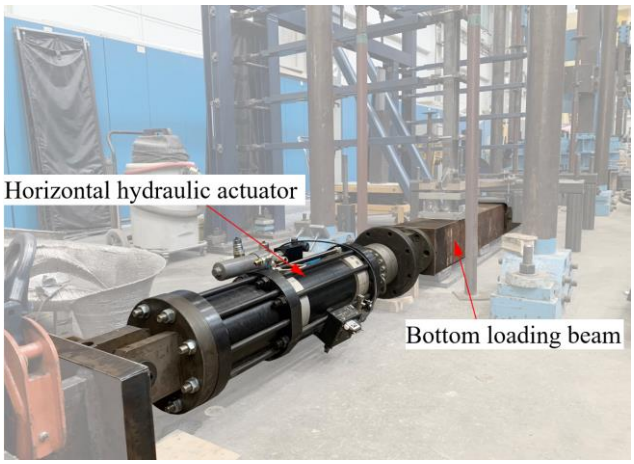
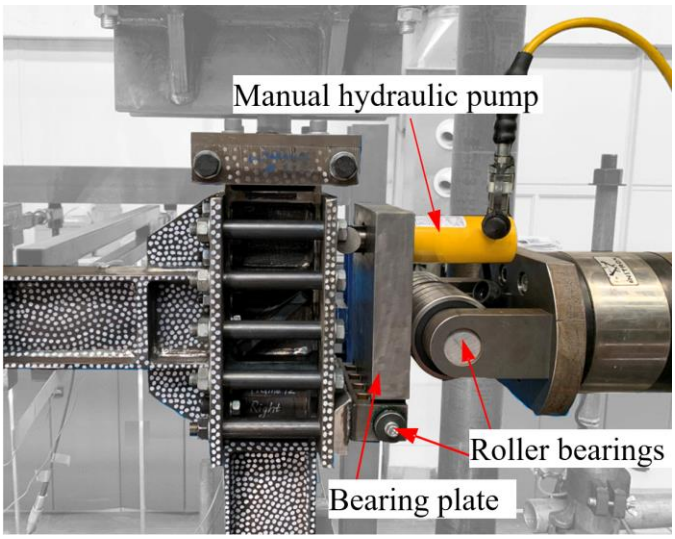
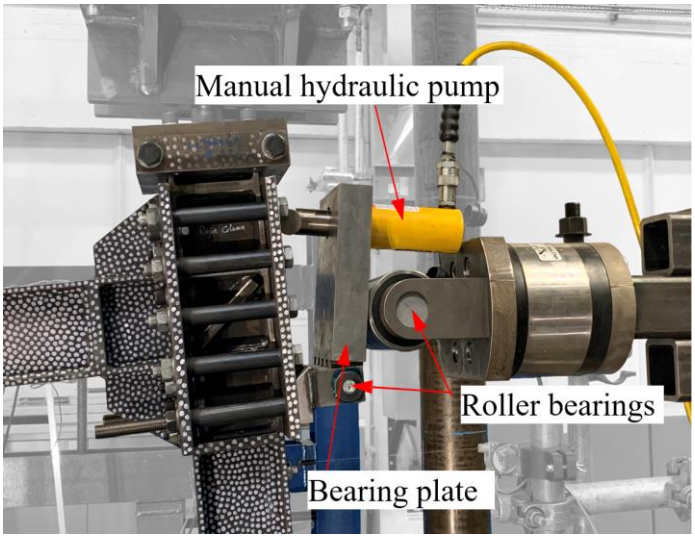


Fig. 8. Horizontal loading system.



(a)



(b)

Fig. 9. Horizontal support (a) prior to testing; and (b) during testing.

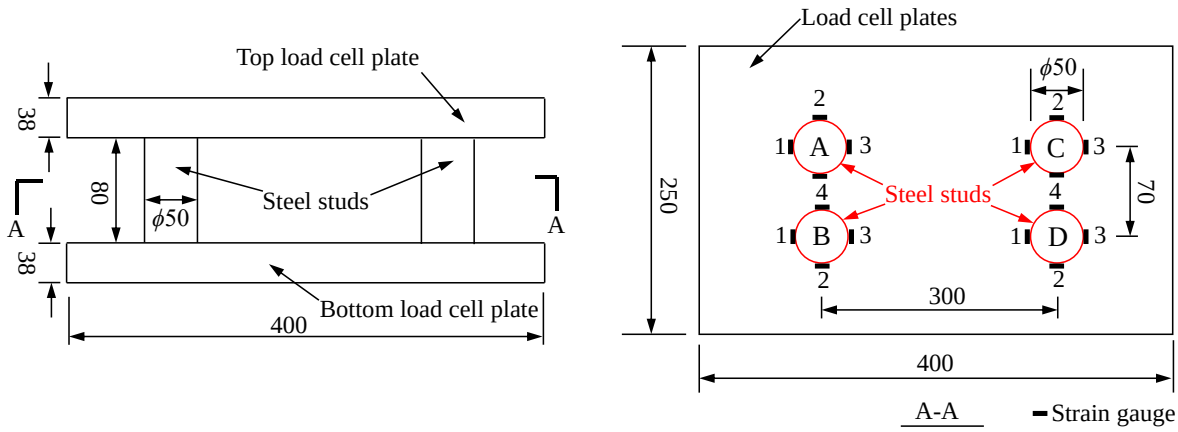
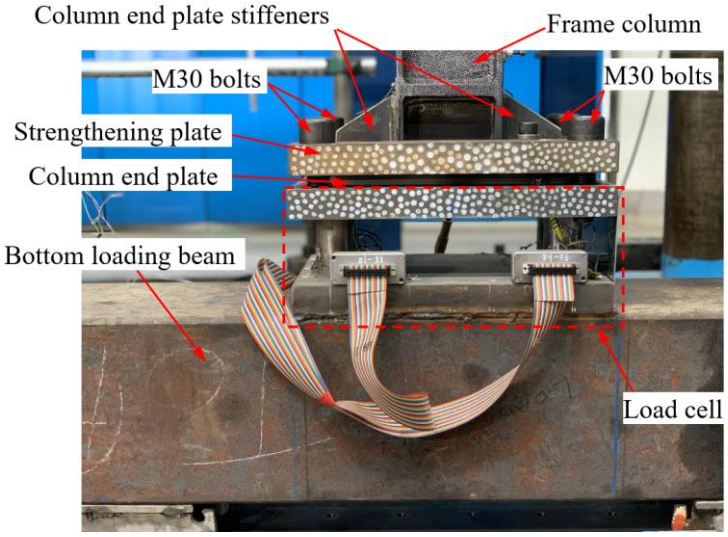
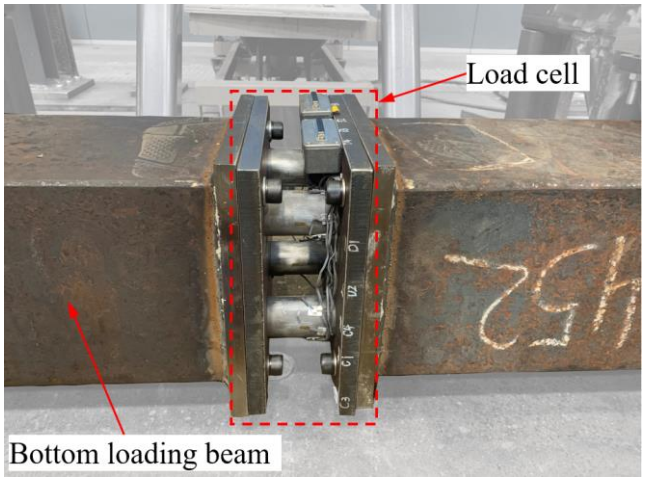


Fig. 10. Dimensions of load cells in mm and arrangement of strain gauges.



(a)



(b)

Fig. 11. Load cells (a) beneath each column and (b) at middle of bottom loading beam.

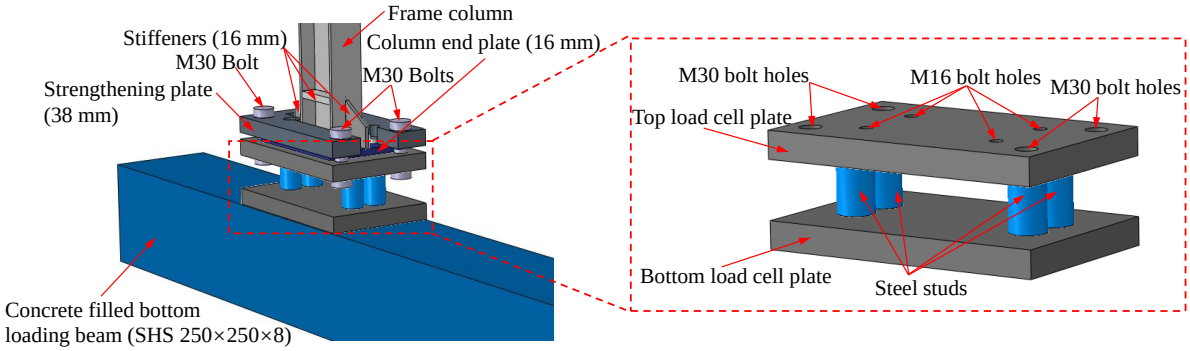
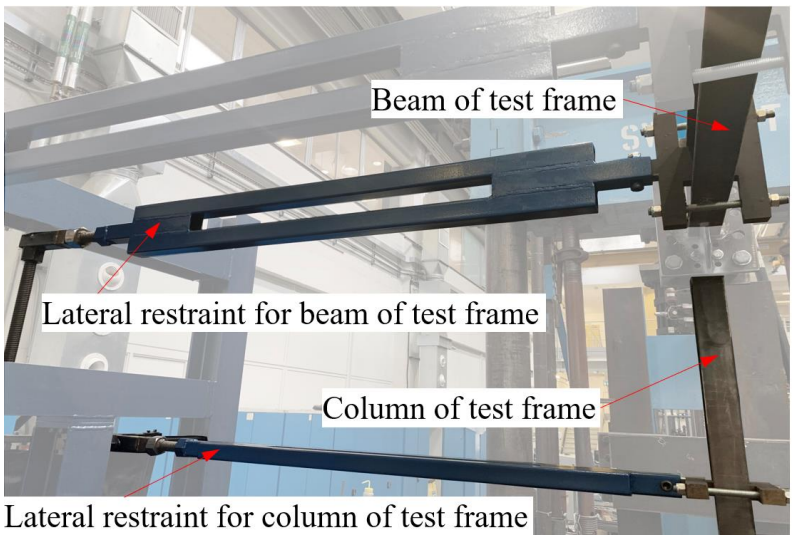
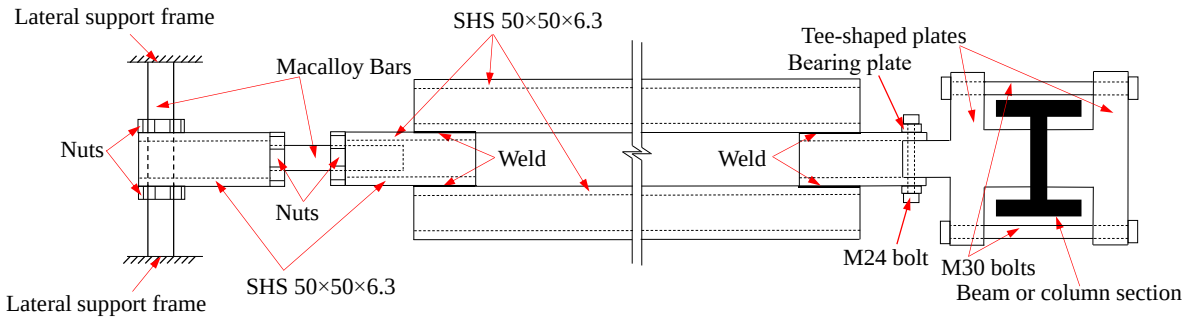


Fig. 12. Schematic solidworks model of column base connection.



(a)



(b)

Fig. 13. Out-of-plane lateral restraints for test frames (a) photo; and (b) schematic drawing.

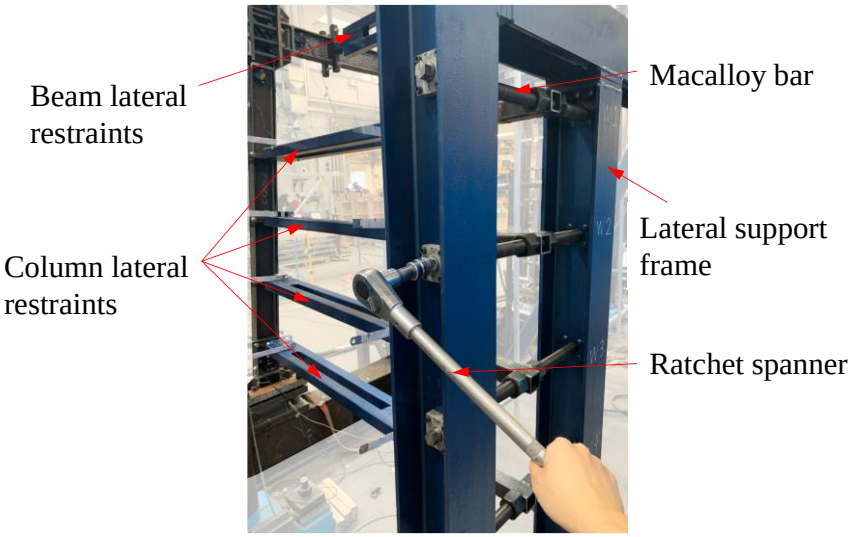


Fig. 14. Adjustment of horizontal position of column lateral restraints.

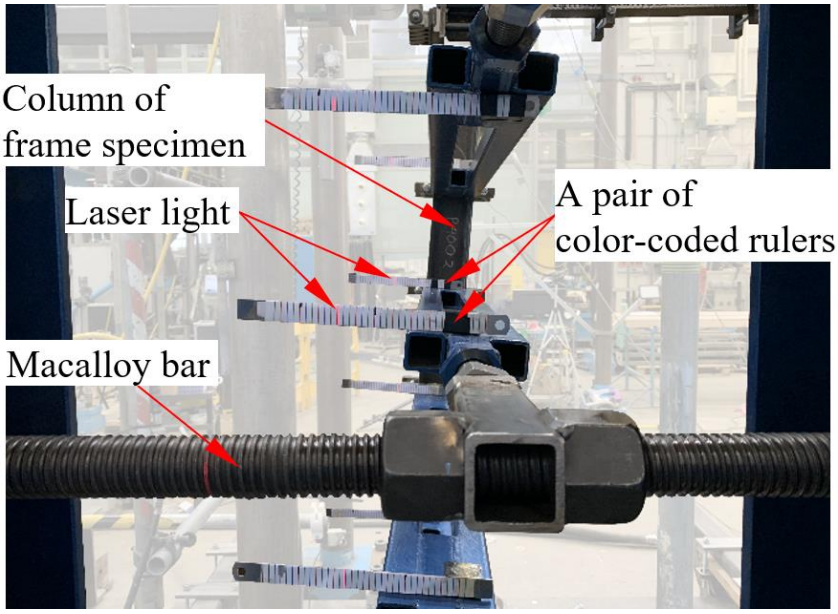


Fig. 15. Use of laser to adjust the position of column lateral restraints.

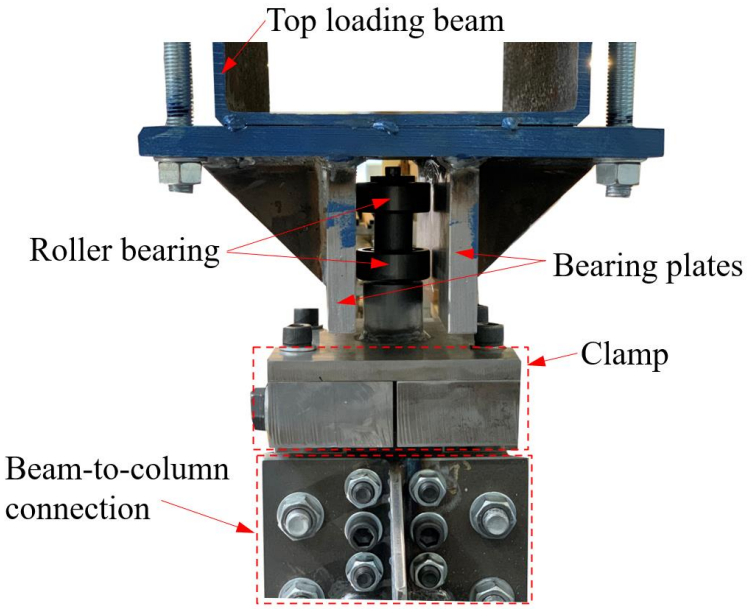


Fig. 16. Lateral restraint at the top ends of the columns.

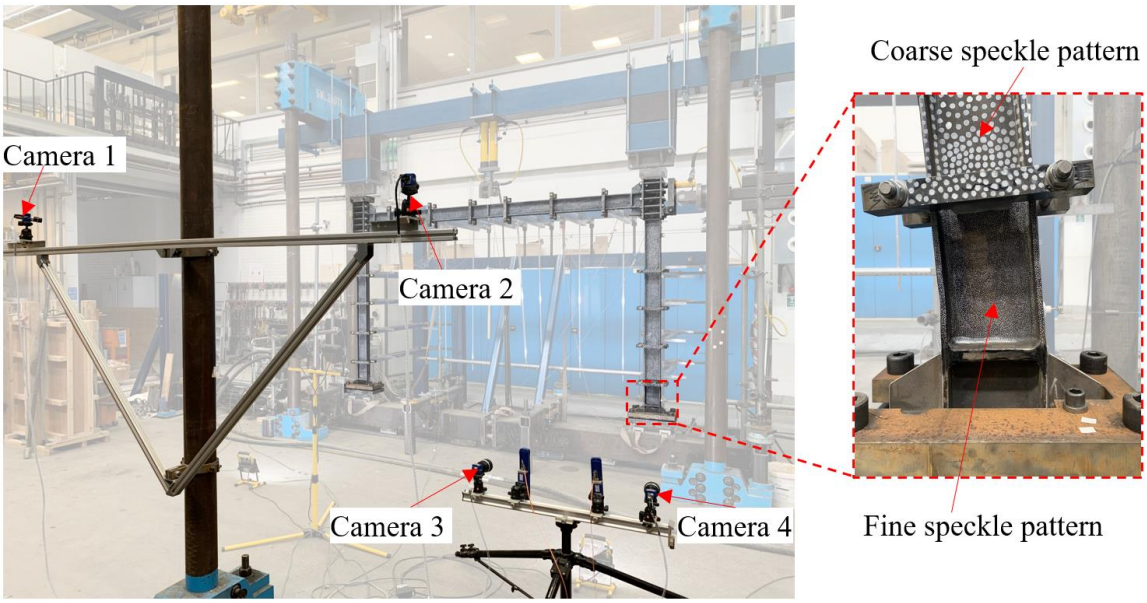
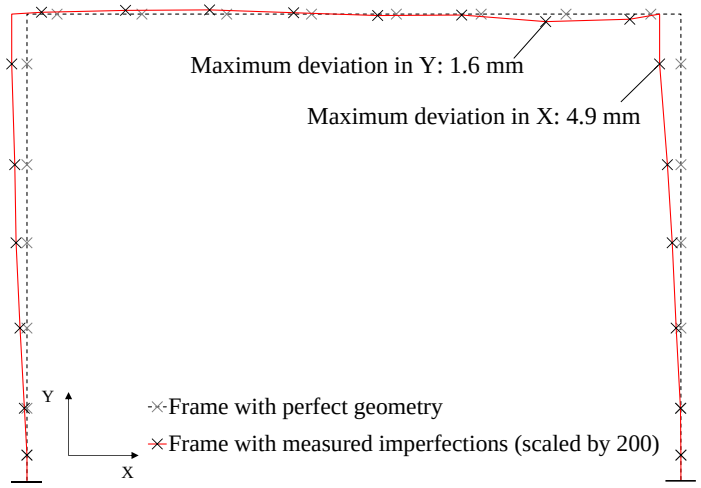
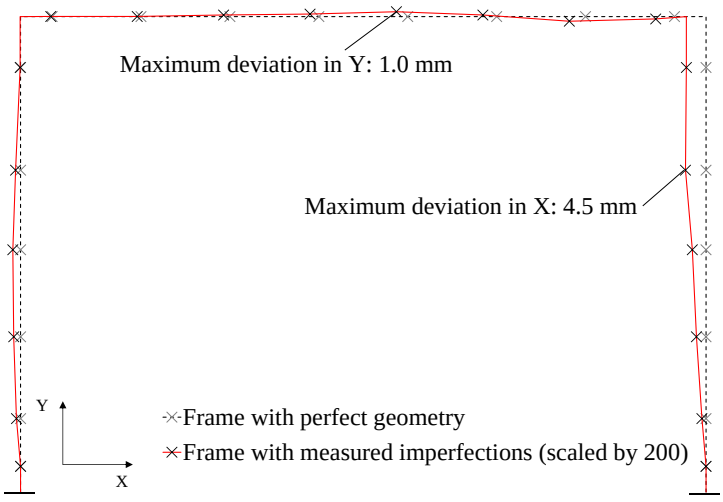


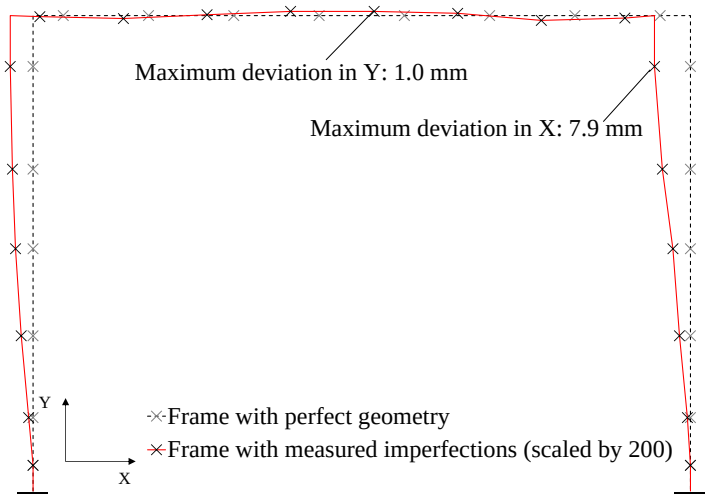
Fig. 17. DIC setup and speckle patterns for frame tests.



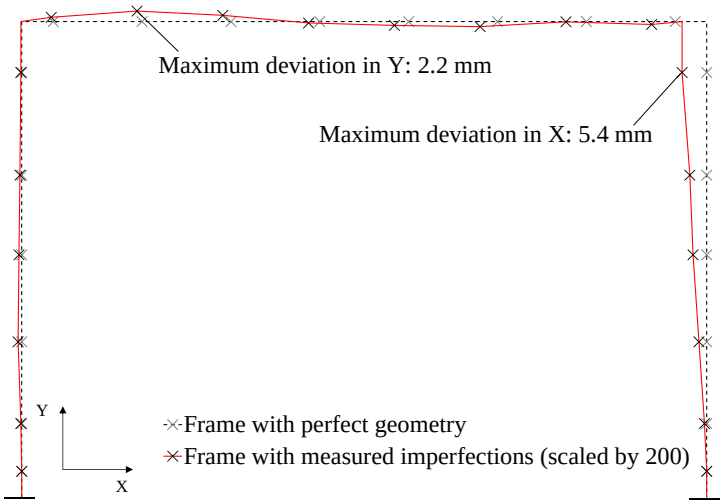
(a)



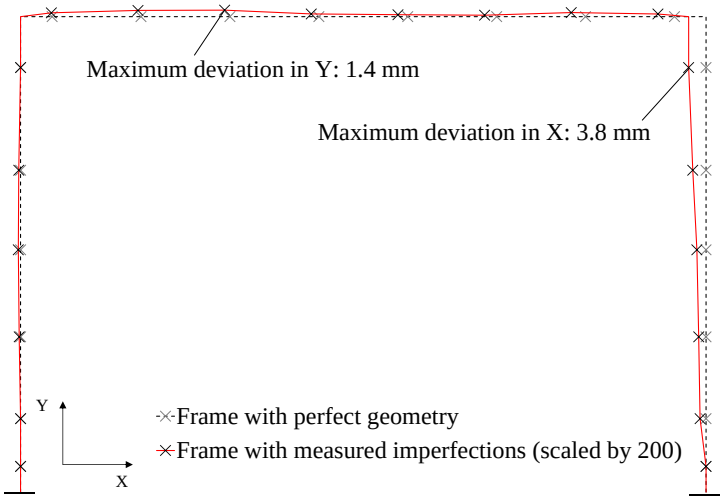
(b)


Maximum deviation in Y: 1.0 mm
Maximum deviation in X: 7.9 mm
Y
X
Frame with perfect geometry
Frame with measured imperfections (scaled by 200)

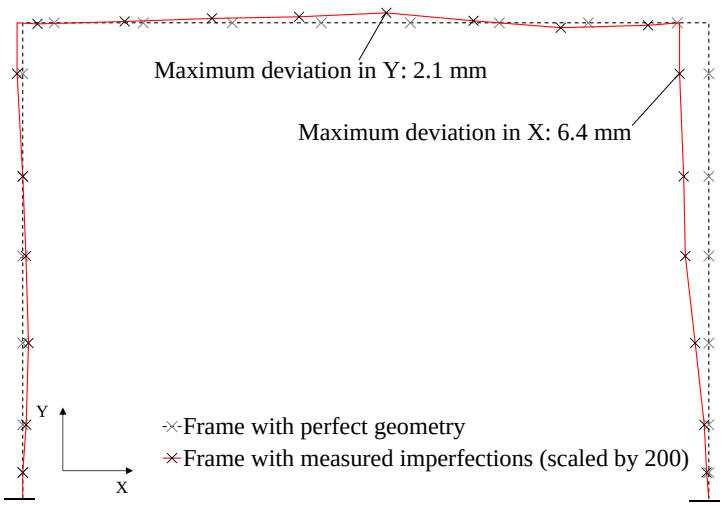
(c)


Maximum deviation in Y: 2.2 mm
Maximum deviation in X: 5.4 mm
Y
X
Frame with perfect geometry
Frame with measured imperfections (scaled by 200)

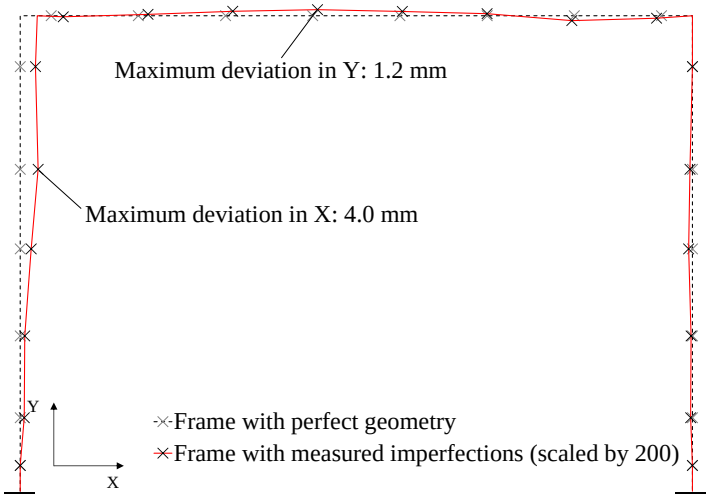
(d)


Maximum deviation in Y: 1.4 mm
Maximum deviation in X: 3.8 mm
Y
X
Frame with perfect geometry
Frame with measured imperfections (scaled by 200)

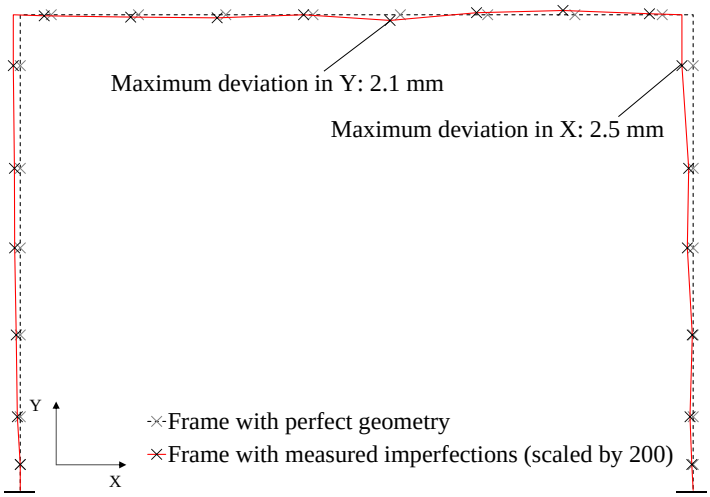
(e)



(f)

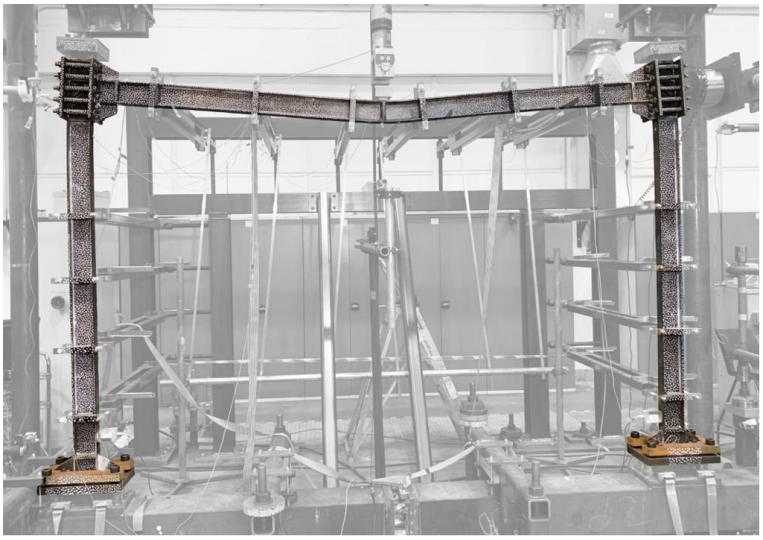


(g)

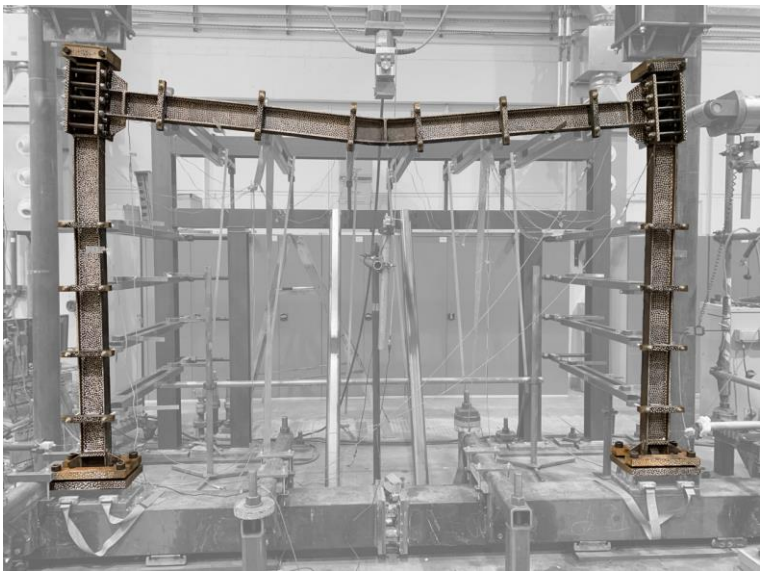


(h)

Fig. 18. Measured in-plane imperfections for frame specimens (a) HSS-I-65×116-V; (b) HSS-I-65×116-H; (c) HSS-I-65×116-V&H-1; (d) HSS-I-65×116-V&H-2; (e) HSS-I-80×136-V; (f) HSS-I-80×136-H; (g) HSS-I-80×136-V&H-1; and (h) HSS-I-80×136-V&H-2.



(a)



(b)

Fig. 19. Failure modes of tested frame specimens subjected to vertical load only (a) HSS-I-65×116-V; and (b) HSS-I-80×136-V.

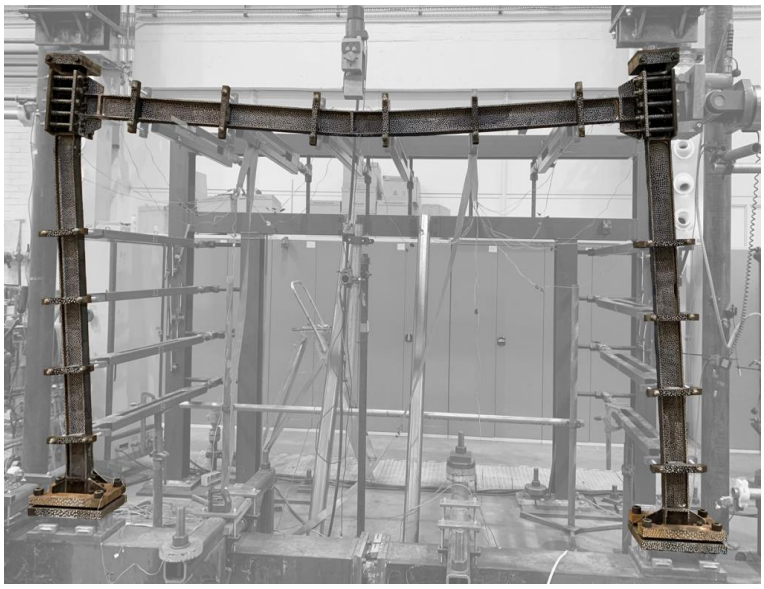


(a)

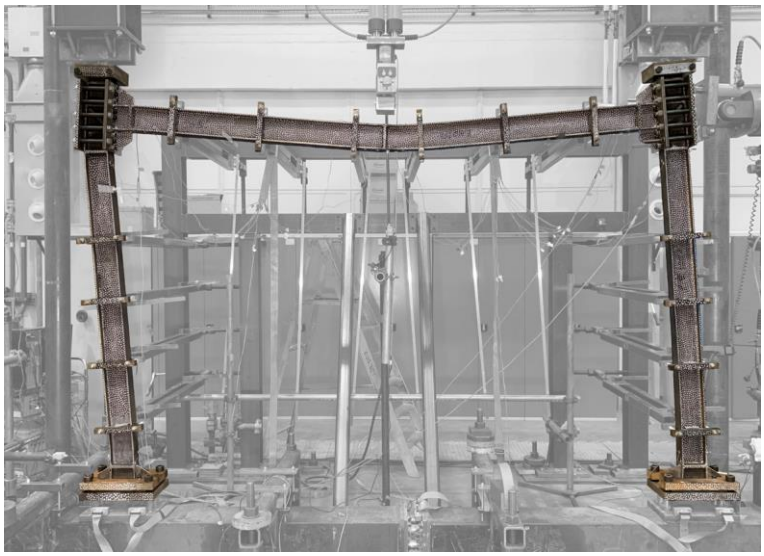


(b)

Fig. 20. Failure modes of tested frame specimens subjected to horizontal load only (a) HSS-I-65×116-H; and (b) HSS-I-80×136-H.



(a)



(b)

Fig. 21. Failure modes of tested frame specimens subjected to the first combination of horizontal and vertical loads (a) HSS-I-65×116-V&H-1; and (b) HSS-I-80×136-V&H-1.



(a)



(b)

Fig. 22. Failure modes of tested frame specimens subjected to the second combination of horizontal and vertical loads (a) HSS-I-65×116-V&H-2; and (b) HSS-I-80×136-V&H-2.

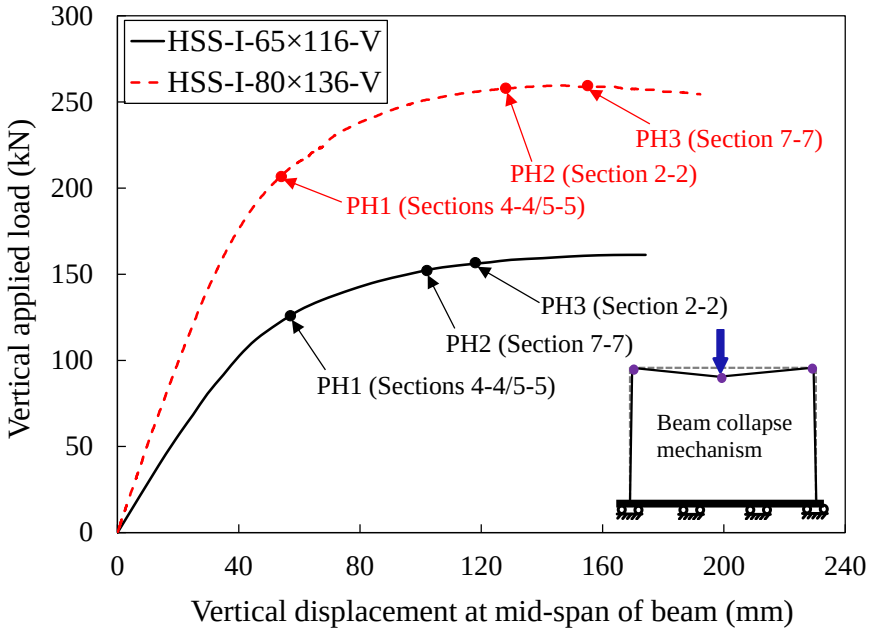


Fig. 23. Vertical load versus mid-span displacement curves and plastic hinge positions for frame specimens subjected to vertical load only.

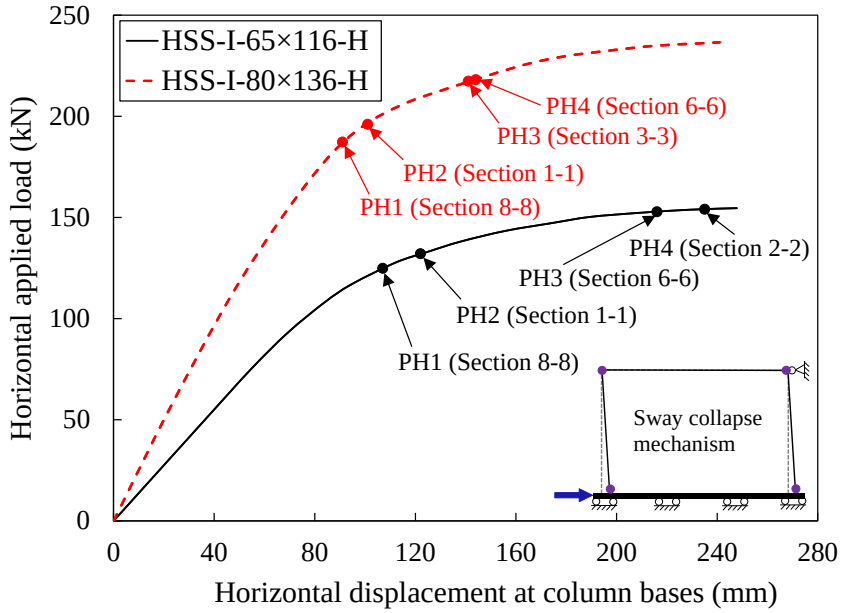
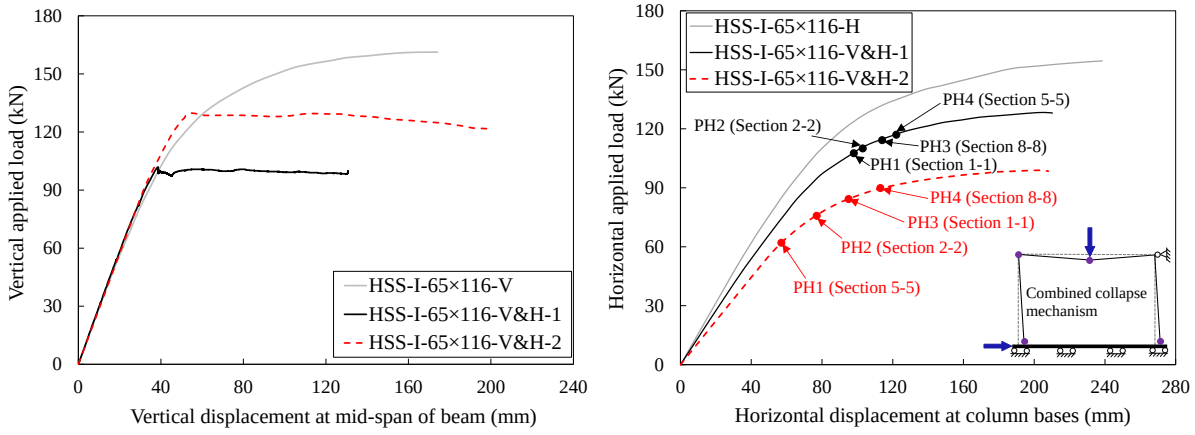
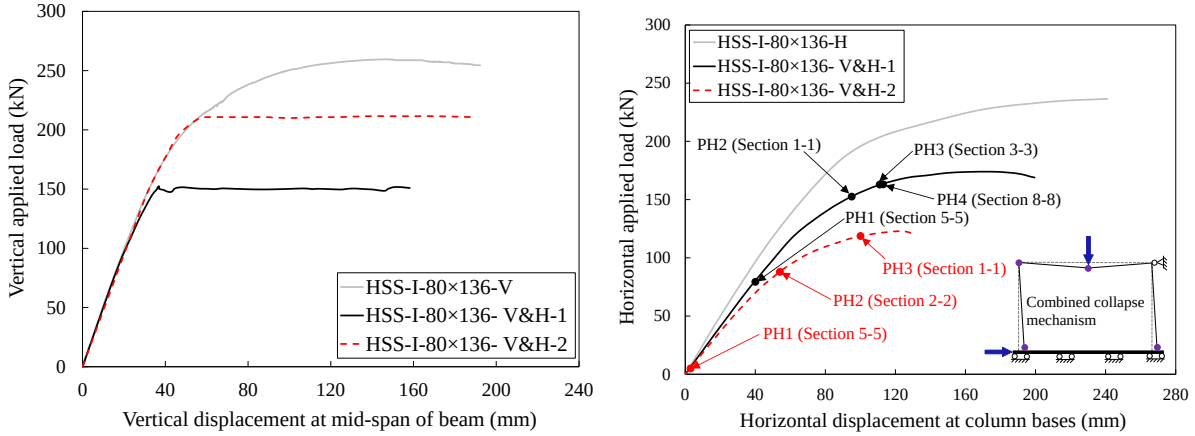


Fig. 24. Horizontal load versus horizontal displacement curves and plastic hinge positions for frame specimens subjected to horizontal load only.

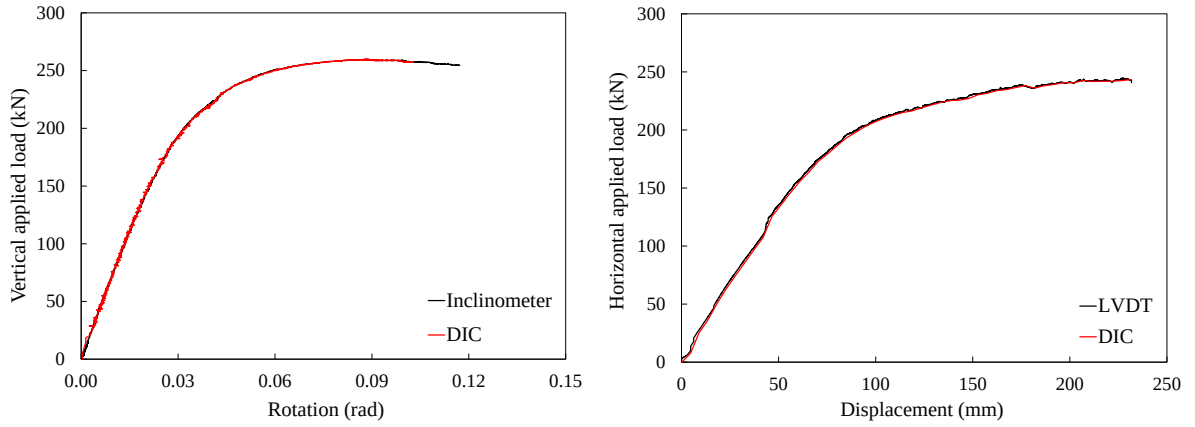


(a)



(b)

Fig. 25. Load-displacement curves and plastic hinge positions for frame specimens subjected to combined vertical and horizontal loads (a) HSS-I-65×116-V&H-1 and HSS-I-65×116-V&H-2; and (b) HSS-I-80×136- V&H-1 and HSS-I-80×136- V&H-2.



(a) (b)

Fig. 26. Comparison of typical load-deformation responses obtained from DIC and conventional instrumentation (a) vertical applied load versus rotation measured at the position of inclinometer I3 for frame specimen HSS-I-80×136-V; and (b) horizontal applied load versus horizontal displacement at the column bases measured at the position of string potentiometer SP5 for frame specimen HSS-I-80×136-H.

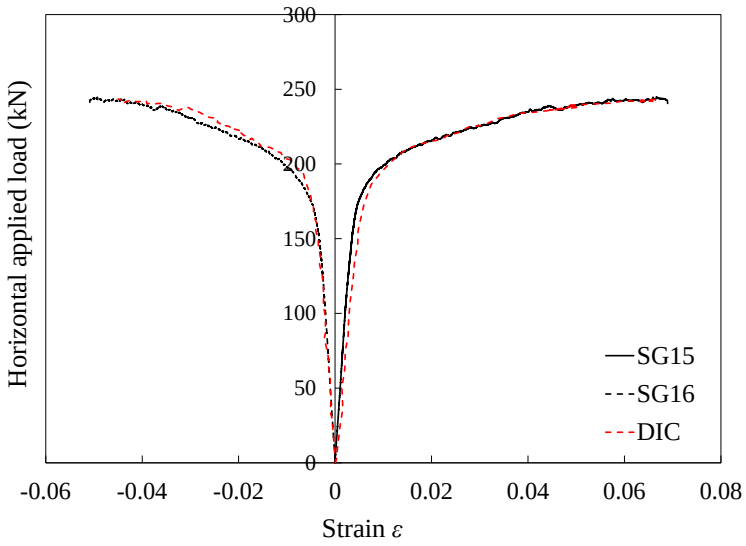
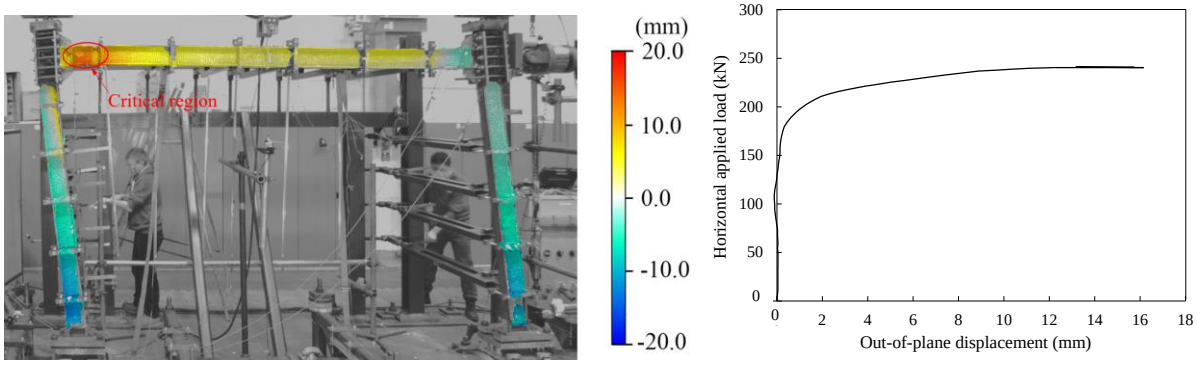
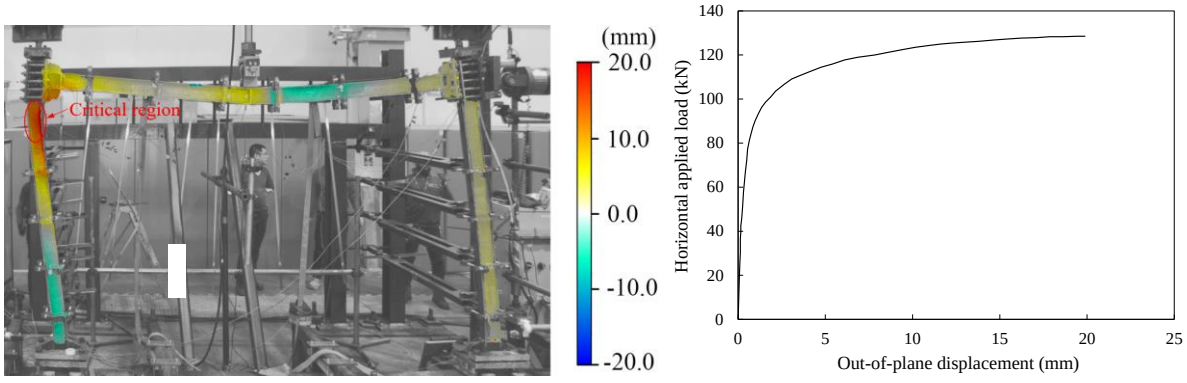


Fig. 27. Comparison of typical histories of strain development obtained from DIC and strain gauges at the positions of SG15 and SG16 for frame specimen HSS-I-80×136-H.



(a)



(b)

Fig. 28. Out-of-plane displacement fields at maximum applied load and load-out-of-plane displacement curves at the critical region of three typical frame specimens obtained from DIC (a) HSS-I-80×136-H; and (b) HSS-I-65×116-V&H-1.

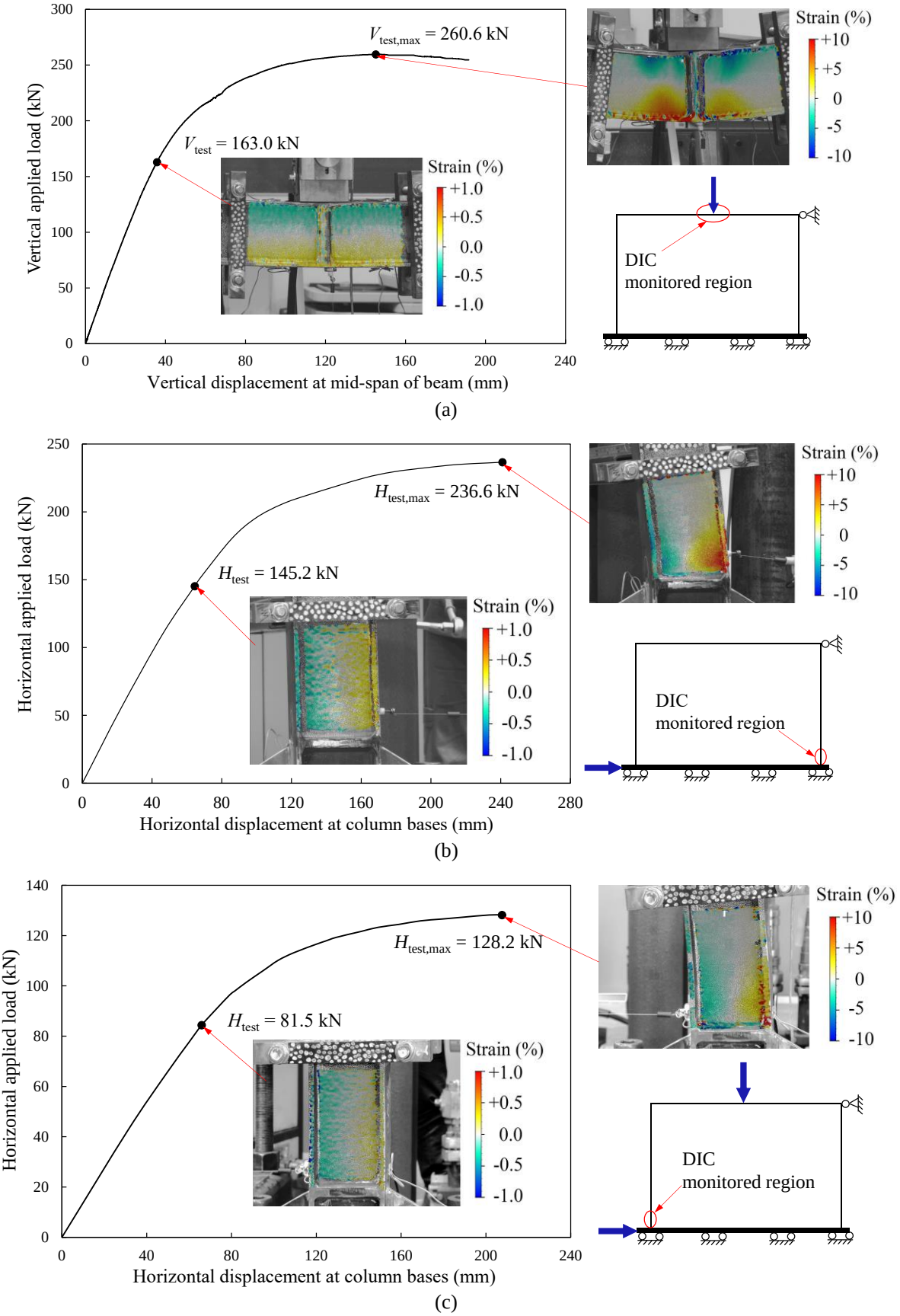


Fig. 29. Longitudinal strain fields at different representative loads obtained from DIC for three typical frame specimens (a) HSS-I-80×136-V, (b) HSS-I-80×136-H; and (c) HSS-I-65×116-V&H-1. (Note that positive strains are tensile and negative strains are compressive).

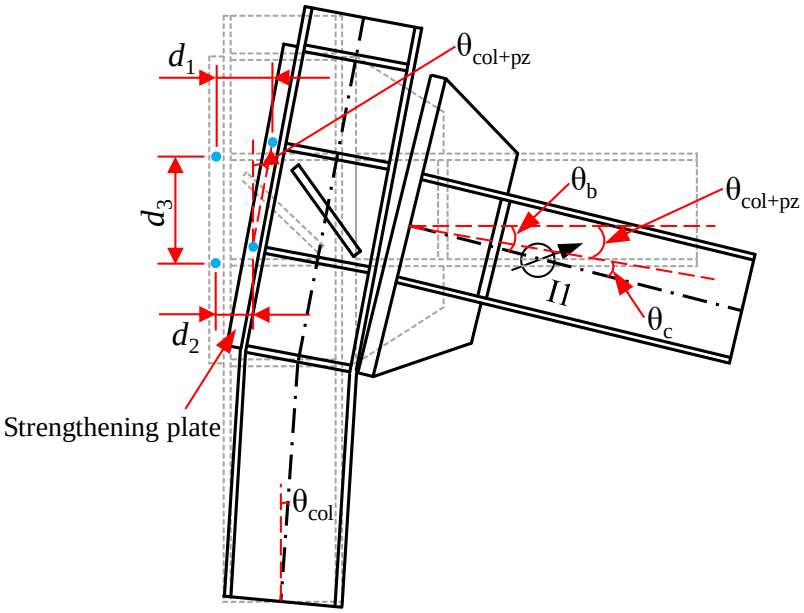


Fig. 30. Schematic illustration of key rotations at the left-hand beam-to-column connection.

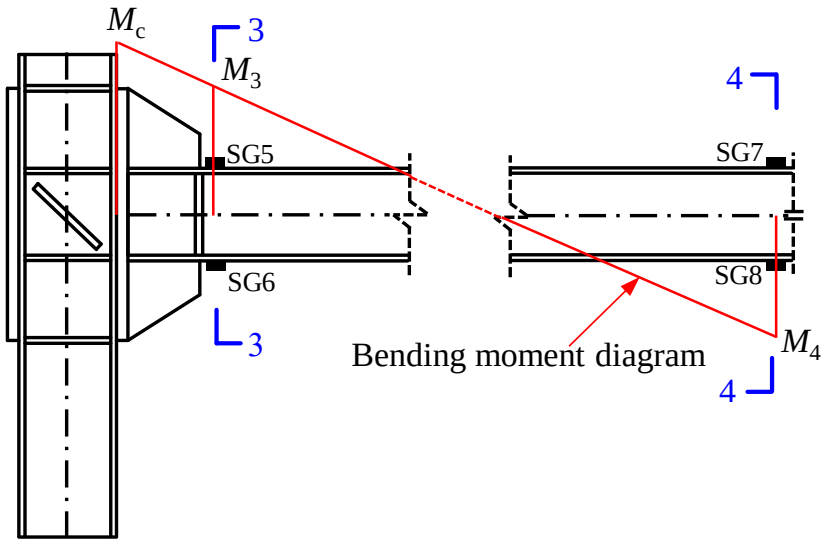


Fig. 31. Illustration of linear interpolation to estimate bending moment at the left-hand beam-to-column connection.

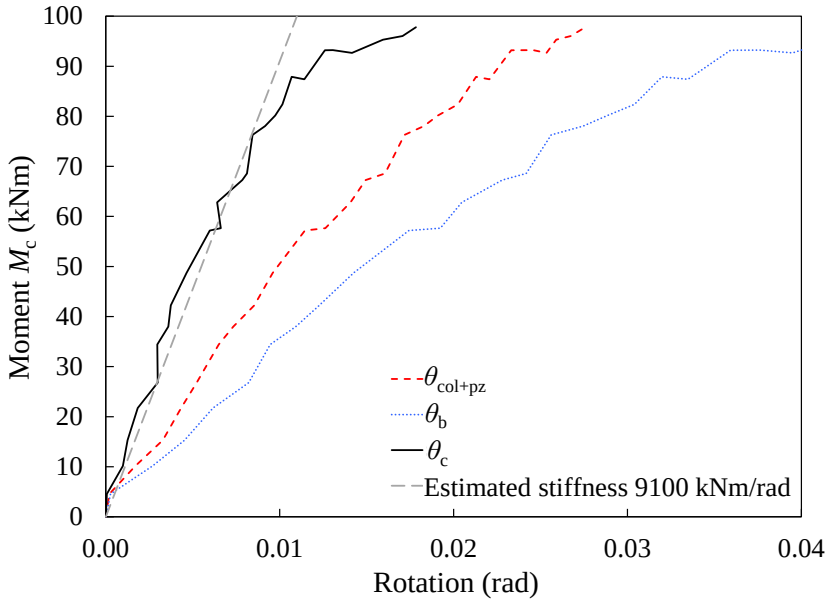


Fig. 32. Moment-rotation curves for left-hand beam-to-column connection of frame specimen HSS-I-80×136-H.

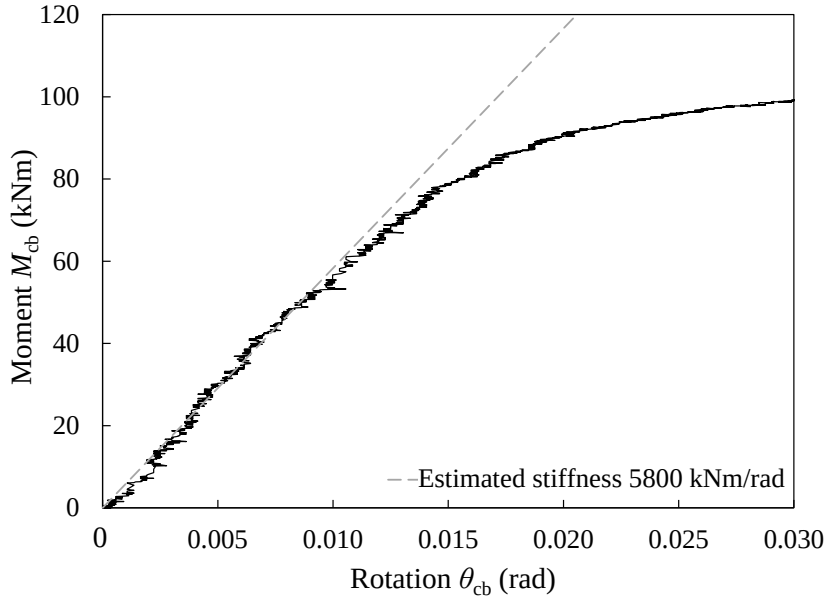


Fig. 33. Moment-rotation curve for left-hand column-base connection of frame specimen HSS-I-80×136-H.

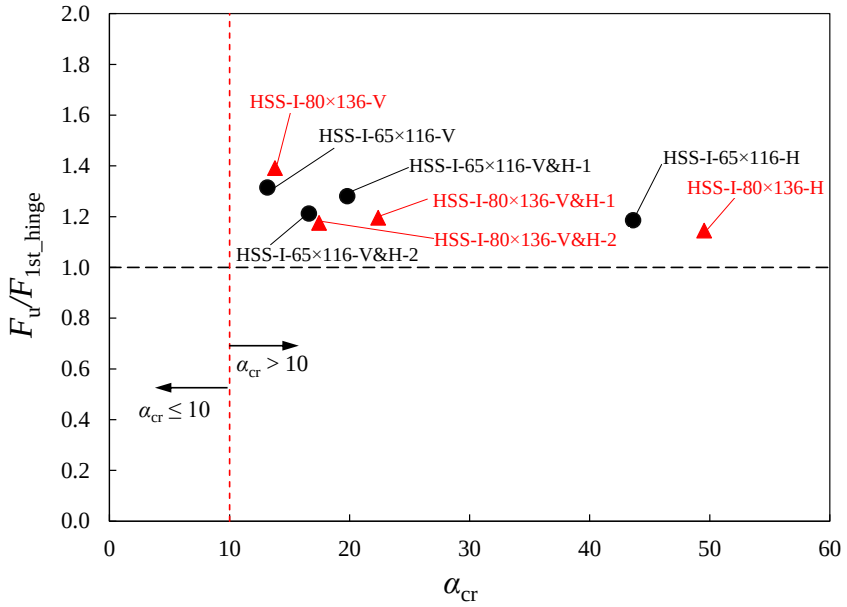


Fig. 34. Ratios of F_u/F_{1st_hinge} versus α_{cr} for the tested frame specimens.

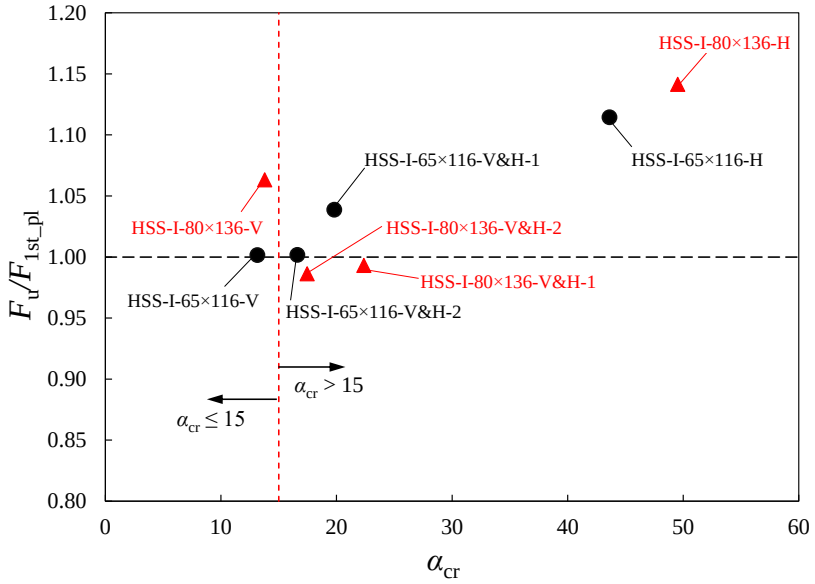


Fig. 35. Ratios of F_u/F_{1st_pl} versus α_{cr} for the tested frame specimens.

Tables

Table 1. Chemical composition of S690 steel employed in the present study.

Steel grade	C	Si	Mn	P	S	N	Cu	Mo	Ni	Cr	V	Nb	Ti	B	Zr	Al
	%	%	%	%	%	%	%	%	%	%	%	%	%	%	%	%
S690	0.139	0.284	1.436	0.013	0.0007	0.0029	0.026	0.068	0.029	0.323	0.002	0.022	0.011	0.0016	0.0002	0.031

Table 2. Key measured material properties obtained from tensile coupon tests.

Steel grade	E	f_y	f_u	ε_{sh}	ε_u	ε_f	f_u/f_y	$\varepsilon_u/\varepsilon_y$
	N/mm^2	N/mm^2	N/mm^2	%	%	%	-	-
S690	212000	782.5	828.4	0.96	6.17	17.3	1.06	16.7

Table 3. Average measured geometric dimensions and cross-sectional properties of frame specimens.

Series	Frame label	B	H	t_f	t_w	t_{weld}	A	W_{el}	W_{pl}	M_{el}	M_{pl}
		mm	mm	mm	mm	mm	mm^2	mm^3	mm^3	kNm	kNm
Series 1	HSS-I-65×116-V	63.64	115.20	8.31	8.21	5.21	1921.3	6.607×10^4	7.905×10^4	51.70	61.86
	HSS-I-65×116-H	64.10	115.73	8.41	8.29	5.52	1959.1	6.770×10^4	8.103×10^4	52.98	63.41
	HSS-I-65×116-V&H-1	64.08	115.79	8.36	8.22	4.96	1934.9	6.696×10^4	8.007×10^4	52.40	62.66
	HSS-I-65×116-V&H-2	64.00	115.30	8.33	8.24	4.87	1926.5	6.632×10^4	7.933×10^4	51.90	62.08
Series 2	HSS-I-80×136-V	79.06	136.77	8.47	8.39	5.61	2407.6	1.014×10^5	1.197×10^5	79.35	93.66
	HSS-I-80×136-H	79.63	136.46	8.51	8.42	5.56	2422.8	1.020×10^5	1.203×10^5	79.80	94.15
	HSS-I-80×136-V&H-1	78.20	136.76	8.36	8.26	5.11	2351.2	9.893×10^4	1.167×10^5	77.42	91.35
	HSS-I-80×136-V&H-2	79.02	136.60	8.35	8.28	4.92	2360.8	9.939×10^4	1.172×10^5	77.77	91.72

Table 4. Summary of maximum applied loads and the corresponding displacements for frame specimens.

Series	Frame label	Vertical loading step		Horizontal loading step	
		$V_{test,max}$	δ_{mid}	$H_{test,max}$	δ_{base}
		kN	mm	kN	mm
Series 1	HSS-I-65×116-V	161.9	173.5	-	-
	HSS-I-65×116-H	-	-	154.5	247.8
	HSS-I-65×116-V&H-1	101.3	38.7	128.2	207.6
	HSS-I-65×116-V&H-2	130.3	54.0	94.6	204.9
Series 2	HSS-I-80×136-V	260.6	143.4	-	-
	HSS-I-80×136-H	-	-	236.6	244.0
	HSS-I-80×136-V&H-1	152.7	37.0	173.9	174.6
	HSS-I-80×136-V&H-2	210.6	58.3	125.2	129.5

Table 5. Summary of maximum measured tensile strains and the corresponding locations.

Series	Frame label	Largest tensile strain		Second largest tensile strain		Third largest tensile strain		Fourth largest tensile strain	
		Location	Value (%)	Location	Value (%)	Location	Value (%)	Location	Value (%)
Series 1	HSS-I-65×116-V	SG10 (SG8)	8.51 (5.97)	SG13 (SG11)	3.07 (0.36)	SG3 (SG5)	1.86 (0.33)		
	HSS-I-65×116-H	SG15	5.41	SG2	4.94	SG12 (SG14)	1.38 (0.49)	SG3 (SG5)	1.13 (0.97)
	HSS-I-65×116-V&H-1	SG2	3.82	SG3 (SG5)	3.11 (1.17)	SG15	2.87	SG10 (SG8)	2.27 (1.89)
	HSS-I-65×116-V&H-2	SG10 (SG8)	5.60 (2.26)	SG3 (SG5)	4.82 (0.99)	SG2	4.29	SG15	2.62
Series 2	HSS-I-80×136-V	SG8 (SG10)	6.86 (5.27)	SG3 (SG5)	2.04 (0.60)	SG13 (SG11)	1.76 (0.49)		
	HSS-I-80×136-H	SG15	6.90	SG2	4.33	SG5 (SG3)	2.21 (0.87)	SG12 (SG14)	1.93 (0.43)
	HSS-I-80×136-V&H-1	SG10 (SG8)	5.90 (2.40)	SG2	4.12	SG5 (SG3)	2.83 (2.43)	SG15	2.58
	HSS-I-80×136-V&H-2	SG10 (SG8)	6.38 (4.68)	SG3 (SG5)	4.62 (1.43)	SG2	2.09	SG15	0.51

Table 6. Average rotational stiffnesses of connections for the tested frames.

Series	Frame label	Beam-to-column connections	EN 1993-1-8 [30] limit for rigid beam-to-column connections	Column-base connections	EN 1993-1-8 [30] limit for rigid column-base connections
		kNm/rad	kNm/rad	kNm/rad	kNm/rad
Series 1	HSS-I-65×116-V	3100	6300	3900	11600
	HSS-I-65×116-H	8400		4200	
	HSS-I-65×116-V&H-1	7900		4000	
	HSS-I-65×116-V&H-2	8200		4400	
Series 2	HSS-I-80×136-V	7100	10900	4200	20100
	HSS-I-80×136-H	8800		5800	
	HSS-I-80×136-V&H-1	8900		5900	
	HSS-I-80×136-V&H-2	8200		5900	